Supplementary Materials for

"Heterogeneous atomic environments destabilize defect clustering to enable a radiation-tolerant alloy"

Tan Shi[1†], Jinxue Yang[1†], Kaihui Xun[2†], Jing Li[1], Bozhao Zhang[2], Zhengxiong Su[1], Huiqiu Deng[3], Jie Hou[4], Xi Qiu[5], Yuanming Li[5], Lu Wu[5], Yongduo Sun[5], Yankun Dou[6], Ke Jin[7,8], Chenyang Lu[1,9*], Jun Ding[2*], Evan Ma[2*]

[1]School of Nuclear Science and Technology, Xi'an Jiaotong University, Xi'an, Shaanxi 710049, China

[2]Center for Alloy Innovation and Design, State Key Laboratory for Mechanical Behavior of Materials, Xi'an Jiaotong University, Xi'an, Shaanxi 710049, China

[3]School of Physics and Electronics, Hunan University, Changsha, Hunan 410082, China

[4]College of Materials Science and Engineering, State Key Laboratory of Cemented Carbide, Hunan University, Changsha 410082, China

[5]Nuclear Power Institute of China, Chengdu, Sichuan 610213, China

[6]China Institute of Atomic Energy, Beijing 102413, China

[7]School of Interdisciplinary Science, Beijing Institute of Technology, Beijing 100081, China

[8]School of Materials Science and Engineering, Beijing Institute of Technology, Beijing 100081, China

[9]State Key Laboratory of Multiphase Flow in Power Engineering, Xi'an Jiaotong University, Xi'an, Shaanxi 710049, China

∗ Corresponding author(s). E-mail(s): chenylu@xjtu.edu.cn (Chenyang Lu), dingsn@xjtu.edu.cn (Jun Ding), maen@xjtu.edu.cn (Evan Ma)

† These authors contributed equally to this work.

Contents

Section 1. Supplementary results on irradiation experiments and defect characterization

1.1 SRIM calculations of displacement per atom

Fig. S1 presents the distributions of displacement per atom (dpa) and incident ion range as functions of sample depth in Nb, Nb-1Zr, and NbZrTi, using both the quick calculation mode and full cascade mode from SRIM calculations. As the quick calculation mode has been frequently employed for radiation damage calculations in previous studies, it is used here to facilitate comparison with other studies. Although the full-cascade calculation mode properly accounts for energy partitioning in multi-elemental targets, its treatment of damage generation near the displacement threshold energy differs substantially from the conventional methods, including the Norgett-Robinson-Torrens (NRT) model[1]. Recent studies have also proposed analyzing the results from the full cascade mode in a different manner to better account for defect production at low energies by modifying the final energy parameter ("*Efinal"* parameter) in SRIM[2]. This approach was also employed, as shown in Fig. S2, which compares the distributions of dpa and incident ion range from the IRADIA program and the SRIM program with a modified final energy of atoms in the full cascade mode. It is shown that the two programs yield similar dpa profiles and overall magnitudes. Due to the complexity involved in the dpa calculations[3], all calculation methods are presented here (Fig. S1 and Fig. S2) to enable comparison with other studies.

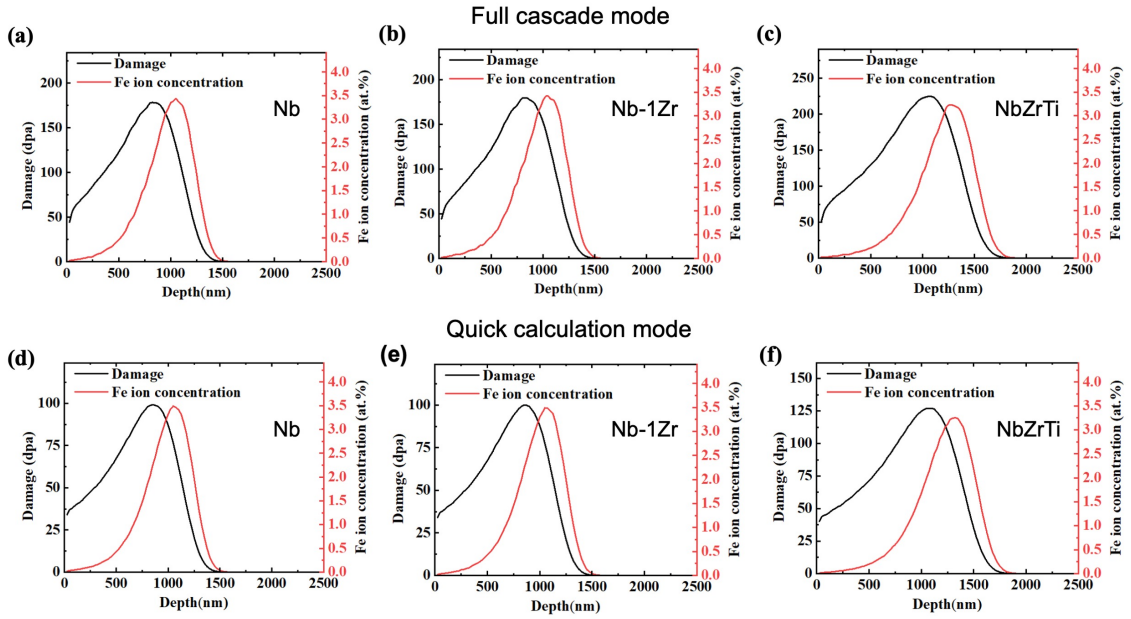

Fig. S1 Distributions of dpa and incident ion range as functions of sample depth from SRIM calculations for Nb, Nb–1Zr, and NbZrTi with 3-MeV Fe ion irradiation at a fluence of 10^{17} ions/cm^2: panels (a–c) show full-cascade mode and panels (d–f) show quick calculation mode.

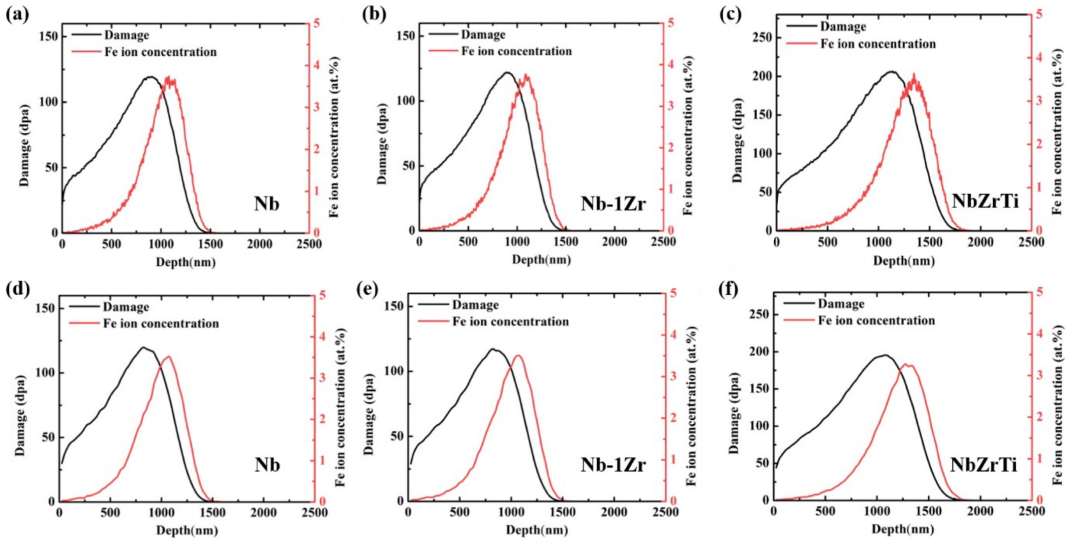

5

Fig. S2 Distributions of dpa and incident ion range as functions of sample depth from IRADIA and SRIM calculations with a modified final energy of atoms in the full-cascade mode for Nb, Nb–1Zr, and NbZrTi with 3-MeV Fe ion irradiation at a fluence of 10^{17} ions/cm^2: panels (a–c) show IRADIA calculations and panels (d–f) show SRIM calculation results.

1.2 Defect characterization of irradiation experiments

Table S1 presents the average size and density of dislocation loops and voids in the enlarged regions in Fig. 1 of the main article after 3 MeV Fe ion irradiation at a fluence of 10^{17} ions/cm^2. An increase in the sizes of voids and dislocation loops is observed in both Nb and Nb-1Zr with increasing temperature. For Nb-1Zr, the absence of voids and the appearance of high-density dislocation loops are consistent with Ref.[4]. showing that the irradiated temperature is close to the lower bound of the swelling regime. Void swelling typically occurs within an intermediate range of homologous temperature (T/T_m). At low temperatures, swelling is kinetically constrained by limited vacancy diffusion; at high temperatures, thermal emission from voids inhibits their growth. The melting point of Nb-1Zr (2683 K) is higher than that of NbZrTi, which was calculated to be 1960 K based on theoretical calculations and 1955 K[5] from our differential scanning calorimetry measurement. Therefore, at the studied irradiation temperatures (873 K and 1023 K), the homologous temperatures of NbZrTi fall within the swelling range, whereas that of Nb-1Zr is just below the void swelling temperature range.

Table S1 Statistical analysis of the average size and density of dislocation loops and voids in the enlarged regions in Fig. 1 in Nb, Nb-1Zr, and NbZrTi after irradiation at 873 K and 1023 K.

	Dislocation loops				**Voids**			
Material	Average size (nm)		Density (m^{-3})		Average size (nm)		Density (m^{-3})	
	873 K	1023 K	873 K	1023 K	873 K	1023 K	873 K	1023 K
Nb	43.5±18.1	99.2±35.3	7.9×10^{20}	1.58×10^{21}	3.2±0.9	18.6±5.3	4.44×10^{22}	2.53×10^{21}
Nb-1Zr	18.1±8.3	53.2±15.3	6.71×10^{21}	1.81×10^{21}	/	/	/	/
NbZrTi	/	/	/	/	/	/	/	/

Fig. S3 presents the X-ray diffraction (XRD) results of NbZrTi prior to irradiation, showing that the equiatomic NbZrTi alloy has a single-phase BCC structure.

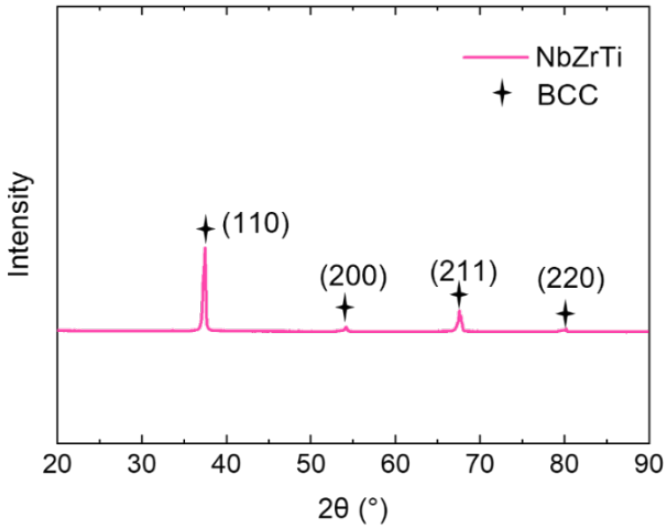

Fig. S3 XRD results of unirradiated NbZrTi.

Section 2. Development of embedded-atom method (EAM) potential for NbZrTi multi-principal element alloy

2.1 Potential formalism

In this study, an EAM potential was developed to describe atomic interactions in medium-entropy alloy NbZrTi with the formalism developed by Zhou *et al.* and Yao *et al.*[6,7]:

$$E = \sum_i F_i(\rho_i) + \frac{1}{2}\sum_{i,j,i\neq j} \emptyset_{ij}(r_{ij}), \quad (1)$$

$$\rho_i = \sum_{j,j\neq i} f_j(r_{ij}), \quad (2)$$

$$f(r) = \frac{f_e \exp\left[-\beta\left(\frac{r}{r_e}-1\right)\right]}{1+\left(\frac{r}{r_e}-\lambda\right)^{20}}, \quad (3)$$

where $F_i(\rho_i)$ is the embedding potential energy of atom i embedded in the local electron density ρ_i, and $\emptyset_{ij}(r_{ij})$ is the two-body potential energy between atoms i and j at a distance r_{ij}. The embedding potential function is described by three separate equations, each corresponding to a specific range of electron density:

$$F(\rho) = \sum_{i=0}^{3} F_{ni}\left(\frac{\rho}{\rho_n}-1\right)^i, \rho < \rho_n, \rho_n = 0.85\rho_e, \quad (4)$$

$$F(\rho) = \sum_{i=0}^{3} F_i\left(\frac{\rho}{\rho_e}-1\right)^i, \rho_n \leq \rho < \rho_o, \rho_o = 1.15\rho_e, \quad (5)$$

$$F(\rho) = F_e\left[1-ln\left(\frac{\rho}{\rho_e}\right)^\eta\right]\cdot\left(\frac{\rho}{\rho_e}\right)^\eta, \rho_o \leq \rho, \quad (6)$$

where f_e, β, r_e, F_e, F_{n0}, F_{n1}, F_{n2}, F_{n3}, F_0, F_1, F_2, F_3 and η are 13 adjustable parameters, ρ and ρ_e are the electron density and equilibrium electron density, respectively. For pure metals, the two-body potential energy between atoms (referred to as A-A interactions) can be expressed as:

$$\phi(r) = \frac{A\cdot exp\left[-\alpha\left(\frac{r}{r_e}-1\right)\right]}{1+\left(\frac{r}{r_e}-\kappa\right)^{20}} - \frac{B\cdot exp\left[-\beta\left(\frac{r}{r_e}-1\right)\right]}{1+\left(\frac{r}{r_e}-\lambda\right)^{20}}, \quad (7)$$

where A, B, α, κ, and λ are fitting parameters.

The formalism proposed by Yao *et al*. was used to describe the two-body term for alloy interactions[8]. Taking the A-B metallic system as an example, the pairwise interaction can be expressed by the following formulation[8]:

$$\phi(r) = \frac{A' \cdot exp\left[-\alpha'\left(\frac{r}{r_{e1}}-1\right)\right]}{1+\left(\frac{r}{r_{e1}}-\kappa'\right)^{n_1}} - \frac{B' \cdot exp\left[-\beta'\left(\frac{r}{r_{e2}}-1\right)\right]}{1+\left(\frac{r}{r_{e2}}-\lambda'\right)^{n_2}}, \quad (8)$$

where A', B', α', β', κ', λ', r_{e1}, r_{e2}, n_1 and n_2 are ten adjustable fitting parameters.

2.2 Database for the potential fitting

An overall summary of the dataset used for potential fitting and validation is provided in Table S2, and a more detailed description on how each physical or defect property was obtained is provided in later subsections. The fitting dataset of pure metals (BCC-Nb, HCP-Zr and HCP-Ti) was obtained from either first-principles calculations or experimental measurements, including lattice constants, cohesive energies, elastic constants, melting point, monovacancy formation energies, divacancy formation energies, and interstitial formation energies. In addition, melting point and vacancy migration energies were used as important defect property indicators to screen the potential function parameters. For binary alloys (BCC-NbTi, BCC-NbZr, and HCP-ZrTi), ten solute or defect properties were considered for each alloy type to fit the cross-interaction parameters. the fitted properties included solute atom formation energies, vacancy formation energies, and interstitial formation energies. for solute atom formation energy, both the formation energy of a single solute atom and 50% of the solute atoms (to consider the energy properties of concentrated alloys) were considered; for vacancy formation energy, configurations with solute atom-vacancy distances of 1NN and 2NN were considered; for interstitial formation energy, both single solute-atom and two solute-atom interstitial types were considered, each including three interstitial structures. Additionally, for the NbZrTi multi-component alloy potential, its lattice constant, melting point, vacancy formation energy, vacancy migration energy, interstitial formation energy, and defect cluster binding energies were compared with first-principles calculation data. This enabled the development of a potential function that accurately reflects the structural and irradiation defect properties of the NbZrTi multi-component alloy.

Table S2 Summary of the dataset for NbZrTi EAM potential, including lattice constant (l_A), cohesive energy (E_c), single and divacancy formation energies E_v^f and E_{2v}^f, vacancy migration energy (E_v^m), elastic constants, melting point (T_m), interstitial formation energies (E_i^f) for various configurations, formation energy of single solute atom ($E_{sub\text{-}B}^f$), formation energy of 50 at.% solute atoms ($E_{sub\text{-}50\%B}^f$), formation energy of vacancy-solute complexes ($E_{vac.\text{-}B}^f$), and formation energy of interstitial-solute complexes ($E_{inter.\text{-}B}^f$). In the AB binary alloy system, element A denotes the matrix atom, while element B represents the solute atom. The target data used for potential fitting are labeled with "F", while the data used for validation are labeled with "V". Data obtained from this study are labeled with "T", while those collected from the literature are labeled with "L".

	Property	Fitting/ validation	Methods	This study/ literature	Material types
Pure metals	l_A (Å)	F	DFT	T	BCC-Nb, HCP-Ti, HCP-Zr
	E_c (eV)	F	DFT	T	
	E_v^f (eV)	F	DFT	T: BCC-Nb; L[9]: HCP-Zr, HCP-Ti	
	$E_{2v\_1NN}^f$ (eV)	F	DFT	T: BCC-Nb; L[9]: HCP-Zr, HCP-Ti	
	E_v^m (eV)	V	DFT	T: BCC-Nb; L[9]: HCP-Zr, HCP-Ti	
	$E_{<i>}^f$ (eV)	F	DFT	T: BCC-Nb; L[10,11]: HCP-Zr, HCP-Ti	
	Elastic constants (Gpa)	F	Experiment	L[10,12,13]	
	T_m (K)	V	Experiment	L	BCC-Nb
Binary alloys	E_{sub-B}^f	F	DFT	T	BCC-NbZr, BCC-NbTi, HCP-ZrTi
	$E_{sub-50\%B}^f$	F	DFT	T	
	$E_{vac.-B}^f$	F	DFT	T	
	$E_{inter.-B}^f$	F	DFT	T	
Multi-principal alloys	$l_{A,\ multi.}$ (Å)	V	DFT	L[14]	BCC-NbZrTi
	$T_{m,\ multi.}$ (K)	V	Phase diagram	L[5]	
	$E_{v,\ multi.}^f$ (eV)	V	DFT	L[14]	
	$E_{v,\ multi.}^m$ (eV)	V	DFT	L[14]	
	$E_{<i>,\ multi.}^f$ (eV)	V	DFT	L[14]	

2.2.1 Property calculations of pure metals

For lattice constants and cohesive energies, unit cells containing two atoms were used for both BCC and HCP pure metal structures, with the Brillouin zone sampled using a 12 × 12 × 12 Monkhorst-Pack (MP) *k*-point mesh. To evaluate defect properties, supercell models were constructed. For BCC Nb, a 128-atom supercell was adopted to calculate the monovacancy formation energy, vacancy migration energy, divacancy formation energy and interstitial formation energy. The supercell volume and atomic coordinates employed in the defect calculations were derived from the fully relaxed perfect crystal obtained through structural optimization. The monovacancy and divacancy formation energies, as well as vacancy migration energies of HCP Zr and HCP-Ti were taken from the previous work[9]. For BCC-Nb, the vacancy migration energies were calculated using the climbing-image nudged elastic band (CI-NEB) method, with a force convergence tolerance of 0.03 eV/Å and three intermediate images. For the calculation of interstitial formation energies, <100>, <110>, and <111> dumbbell interstitial configurations were considered for BCC-Nb in this study. For HCP Zr and HCP Ti, interstitial formation energies were obtained from DFT calculations reported by Vérité et al.[11], which was also calculated with the VASP program under the same first-principles framework with similar simulation settings. Five typical interstitial configurations were considered: octahedral (O), split dumbbell along the c-axis (S), crowdion (C), basal octahedral (BO), and split dumbbell in the basal plane (BS), as schematically shown in Fig. S4. These calculations used a 288-atom supercell and a 3 × 3 × 3 MP mesh in order to better accommodate the local stress field caused by interstitial atoms and reduce finite-size effects. For these defect structures, the defect structural optimization was conducted with the volume scaled by $(N+1)V_0/N$, where N is the number of atoms, V_0 is the initial volume of the perfect crystal. In addition, the melting point of BCC-Nb were obtained from the previous work.

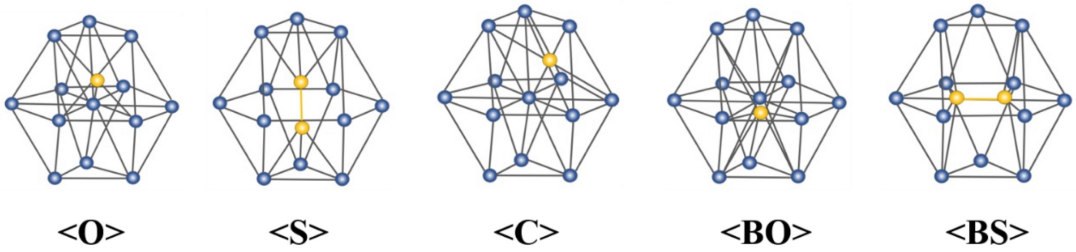

Fig. S4 Schematic diagram of interstitial configurations in the HCP crystal structure.

2.2.2 Property calculations of binary alloys

For Nb-Ti and Nb-Zr interactions, a 4 × 4 × 4 BCC supercell of 128 atoms was used for property and defect calculations. For Zr-Ti interactions, an HCP supercell was used due to the instability of BCC Zr-Ti alloy at ground state, where a 4 × 4 × 3 supercell of 96 atoms was employed for the calculation of solute formation energies and vacancy formation energies, and a 5 × 5 × 3 supercell of 150 atoms was used for the calculation of interstitial formation energies. Brillouin zone sampling was performed using a 3 × 3 × 3 Monkhorst–Pack *k*-point mesh. All structural optimizations were carried out under constant pressure conditions.

The solute formation energies in binary alloys include both dilute alloy (a single substitutional solute) and concentrated alloy (50 at.% solute concentration, see Fig. S5(a)). The formation energy of the later was obtained by averaging over five random solid solution configurations in order to reflect the energy characteristics of concentrated alloys.

The vacancy formation energies involve configurations where the distance between the solute atom and the vacancy corresponds to either the first nearest neighbor (1NN) or the second nearest neighbor (2NN), as shown in Fig. S5. For each of the three binary alloys, six interstitial configurations were considered. The interstitial formation energies include configurations containing one or two solute atoms occupying interstitial sites. Specifically, for Nb-Ti and Nb-Zr, <100>, <110>, and <111> dumbbell configurations were considered. For HCP Zr-Ti, <BO>, <O>, and <S> configurations were considered, with either one solute atom at the interstitial site or an additional solute atom at the interstitial nearest neighbor (see Fig. S6).

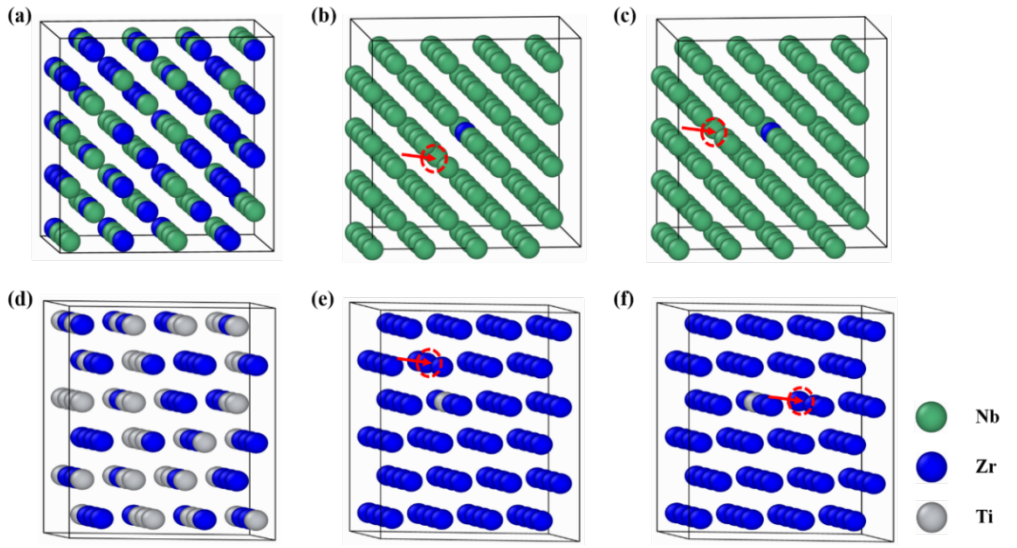

Fig. S5 Representative configurations of 50% solute atoms and vacancy–solute arrangements in (a-c) BCC-NbZr and (d-f) HCP-ZrTi alloys: (a, d) 50% solute atom distributions; (b, c) vacancy-solute configurations with the distance of 1NN and 2NN in BCC-NbZr; (e, f) vacancy-solute configurations with the distance of 1NN and 2NN in HCP-ZrTi.

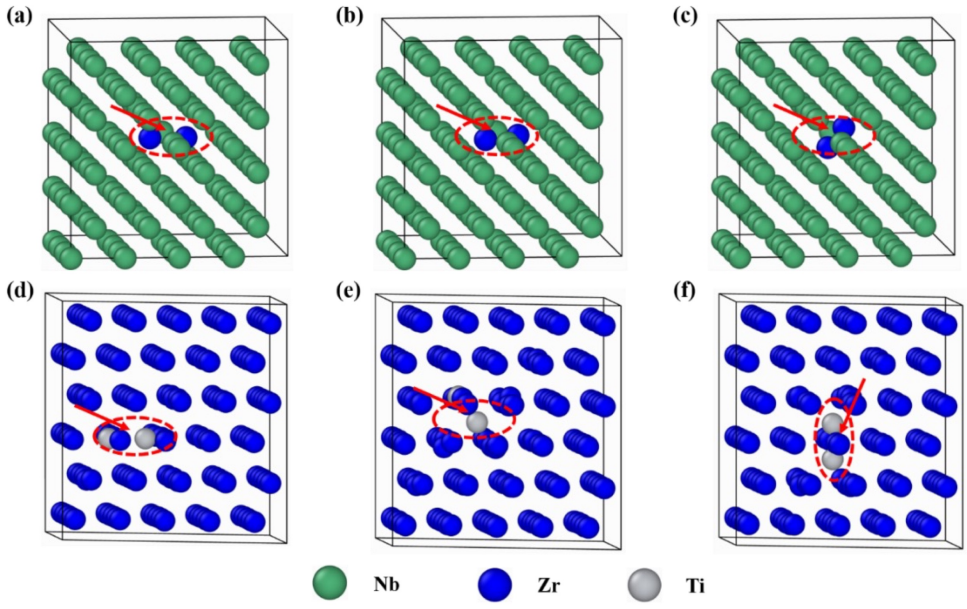

Fig. S6 Interstitial configurations formed by two solute atoms in BCC Nb-Zr and HCP-ZrTi structures: (a–c) BCC-NbZr interstitial configurations along the <100>, <110>, and <111> directions, respectively; (d–f) HCP-ZrTi interstitial configurations corresponding to the <BO>, <O>, and <S> directions, respectively.

The formation energy of a single substitutional solute B atom in an element A matrix is calculated as follows:

$$E^{\mathrm{f}}_{\mathrm{sub_B}} = E_{\mathrm{sub_B}} - (N-1)E^{\mathrm{A}}_{\mathrm{C}} - E^{\mathrm{B}}_{\mathrm{C}}, \tag{9}$$

where $E^{\mathrm{f}}_{\mathrm{sub_B}}$ is the energy of the system in which a solute B atom replaces an A atom in A matrix, $E^{\mathrm{A}}_{\mathrm{C}}$ and $E^{\mathrm{B}}_{\mathrm{C}}$ are the cohesive energies of A and B atoms in the ground state, and *N* is the number of atoms in the structure. The formation energy of the 50% solute B atom in A matrix can be expressed as:

$$E^{\mathrm{f}}_{\mathrm{sub_{50\%B}}} = E_{\mathrm{50\%A+50\%B}} - \frac{N}{2}E^{\mathrm{A}}_{\mathrm{C}} - \frac{N}{2}E^{\mathrm{B}}_{\mathrm{C}}, \tag{10}$$

where $E_{\mathrm{50\%A+50\%B}}$ is the energy of the system in which a solute B atom replaces 50% of the A atoms in A matrix. The formation energy of the defect complex involving a single solute B atom and a single vacancy can be expressed as:

$$E^{\mathrm{f}}_{\mathrm{B-vac.}} = E_{\mathrm{B-vac.}} - (\mathrm{N}-2)E^{\mathrm{A}}_{\mathrm{C}} - E^{\mathrm{B}}_{\mathrm{C}}, \tag{11}$$

where $E_{\mathrm{B-vac.}}$ is the total energy of such a configuration with a distance of 1NN/2NN between the solute atom and the vacancy. The formation energies of the A-B and B-B interstitial atoms in A matrix can be expressed as:

$$E^{\mathrm{f}}_{\mathrm{A-B}} = E_{\mathrm{A-B}} - \mathrm{N}E^{\mathrm{A}}_{\mathrm{C}} - E^{\mathrm{B}}_{\mathrm{C}}, \tag{12}$$

$$E^{\mathrm{f}}_{\mathrm{B-B}} = E_{\mathrm{B-B}} - (\mathrm{N}-1)E^{\mathrm{A}}_{\mathrm{C}} - 2E^{\mathrm{A}}_{\mathrm{C}}, \tag{13}$$

where $E_{\mathrm{A-B}}$ and $E_{\mathrm{B-B}}$ are the energies of the systems containing A-B interstitials and B-B interstitials in A matrix, respectively.

2.3 Potential fitting results

In the potential function fitting process, the EAM potential parameters corresponding to the interatomic interactions of the pure constituent elements (Nb, Zr, and Ti) were first optimized, including 19 parameters for each pure metal (see Section 2.1). This step was followed by fitting cross-interaction parameters for the binary alloy systems (NbTi, NbZr, and ZrTi), including 10 parameters for each binary alloy (see Section 2.1). The target optimization functions for the EAM potential function parameters are as follows:

$$Z_i = \sum_{k=0}^{N} w_k \delta\left(A_k^{\text{predict}}, A_k^{\text{target}}\right)^2 \tag{14}$$

$$\delta\left(x^{\text{predict}}, x^{\text{target}}\right) = \begin{cases} \frac{\left(x^{\text{predict}} - x^{\text{target}}\right)}{x^{\text{target}}}, x^{\text{target}} \neq 0 \\ x^{\text{predict}} - x^{\text{target}}, x^{\text{target}} = 0 \end{cases} \tag{15}$$

where A_k^{predict} and A_k^{target} are the predicted and target values of the k-th property, respectively. In addition, w_k is the weight assigned to the corresponding target property, distinguishing the importance of each fitted target property.

In this study, a combination of global and local optimization algorithms was used to optimize the potential function parameters[15], balancing optimization accuracy and efficiency. The global optimization algorithm used was Simulated Annealing (SA) method, and the local optimization algorithm employed was the Nelder-Mead Simplex method. Table S3 and Table S4 list the fitting parameters for pure element and binary interactions, respectively. As shown in Fig. S7, the potential function curves vary smoothly across the entire range.

Table S3 EAM potential parameters for pure Nb, Zr and Ti.

Parameters	Nb	Zr	Ti
r_e (Å)	2.865678	3.009463	2.840032
f_e (eV/Å)	2.525407	2.797566	1.749626
ρ_e (eV/Å)	27.010559	28.289631	17.486487
α	8.533943	9.762474	8.274178
β	5.313835	3.675897	5.212297
A (eV)	0.655843	0.403517	0.374496
B (eV)	0.996650	0.589293	0.640632
κ	0.108481	0.308468	0.079676
λ	0.481013	0.697019	0.212465
F_{n0} (eV)	-4.335953	-4.499573	-3.481649
F_{n1} (eV)	-0.415344	-0.151667	-0.186161
F_{n2} (eV)	1.463119	0.498592	0.647306
F_{n3} (eV)	-2.457489	-3.849314	-2.648182
F_0 (eV)	-4.365052	-4.513601	-3.496911
F_1 (eV)	0.091523	-0.000996	-0.001598
F_2 (eV)	1.842677	0.312263	0.553509
F_3 (eV)	-0.405335	-0.800548	-0.760925
η	1.005965	0.300000	0.498257
F_e (eV)	-4.358569	-4.512745	-3.496146

Table S4 EAM potential parameters for Nb-Ti, Nb-Zr and Zr-Ti interactions.

Parameters	NbTi	NbZr	ZrTi
A' (eV)	0.665445	0.559240	0.611186
B' (eV)	0.719024	0.693843	0.713390
α'	11.260071	9.511346	8.870863
β'	3.137208	2.761590	4.358476
κ'	0.192048	0.188611	0.139906
λ'	0.570317	0.484131	0.834541
n1	19.600000	19.600000	19.600000
n2	20.200000	20.200000	20.200000

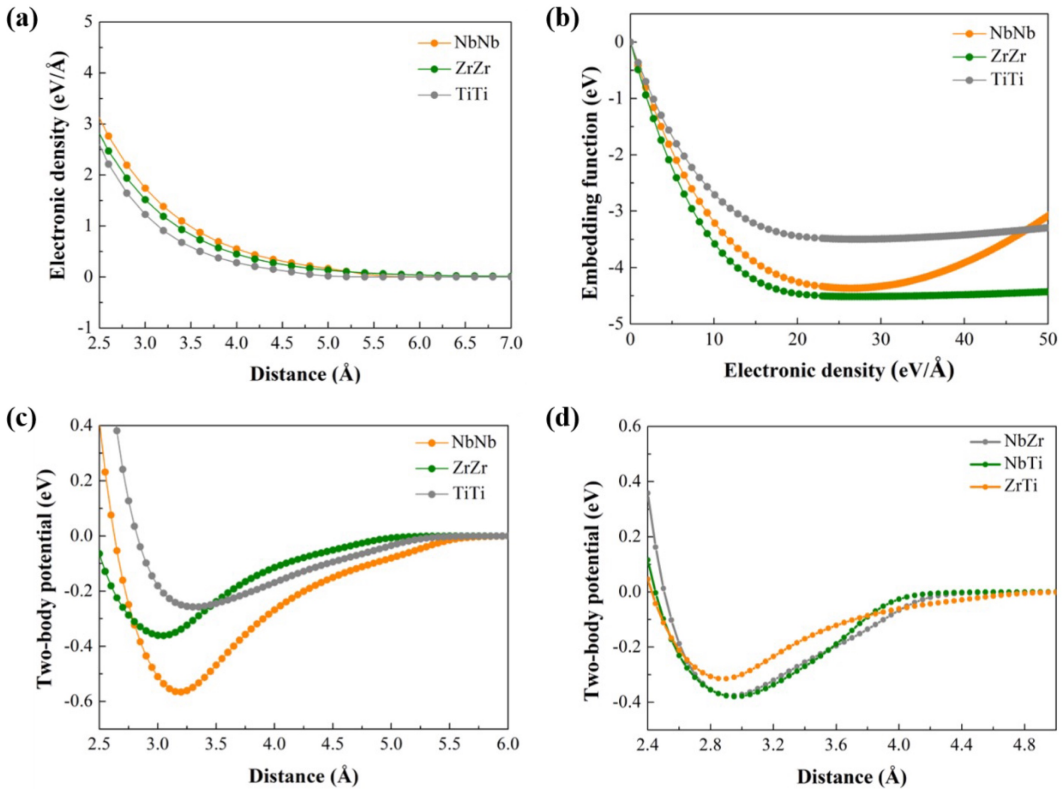

Fig. S7 Dependence of the potential functions on atomic distance or electronic density: (a) Electronic density functions; (b) Embedding energy functions; (c) Pair potentials for pure elements; (d) Pair potentials for binary alloy interactions.

2.4 Potential verification

2.4.1 Pure metals

Table S5 summarizes the physical and defect properties calculated using the developed EAM potential for BCC Nb. The fundamental physical properties of pure Nb, including the lattice constant, cohesive energy, and elastic constants, show good agreement with DFT and experimental data. For defect related properties, including vacancy formation energy, divacancy formation energy, and vacancy migration energy, the deviations from DFT results are generally less than 0.2 eV. Regarding interstitial formation energies, the potential predicts the <111> dumbbell configuration to be the most stable, followed by the <110> dumbbell and <100> dumbbell, which is consistent with the DFT-predicted trend. For most of these configurations, the deviations are less than 0.1/0.2 eV, and in some cases they remain within approximately 0.3 eV. We note that the C_{44} exhibits a relatively large discrepancy; however, this property is sometimes difficult to reproduce in classical potentials[16,17] and is not expected to significantly affect the radiation defect simulations in this study. Overall, the optimized BCC Nb potential shows good agreement with DFT results, laying a solid foundation for the simulations of defect behaviors in BCC Nb.

Table S6 and Table S7 compare the physical properties and defect properties of HCP Zr and HCP Ti, respectively. The results indicate that the fundamental physical properties of Zr and Ti, such as the lattice constant, cohesive energy, and elastic constants, agree well with both DFT and experimental values. The vacancy formation energy, vacancy migration energy, and interstitial formation energy deviate by less than 0.3 eV and 0.2 eV from the DFT results for Zr and Ti, respectively. In particular, the most stable interstitial configuration is predicted to be the BO configuration, which is in agreement with DFT calculations.

Table S5 Summary of the lattice constant (l_A), cohesive energy (E_c), single and divacancy formation energies E_v^f and E_{2v}^f, interstitial formation energies (E_i^f) for various configurations, vacancy migration energy (E_v^m), and elastic constants of BCC Nb. Properties presented in *italics* were not used in the fitting dataset, and those denoted with an asterisk (*) correspond to experimental values.

Property	NbZrTi-EAM potential	DFT/experiment
l_A (Å)	3.31	3.31/3.30* [18]
E_c (eV)	7.14	7.10/7.57* [19]
E_v^f (eV)	2.56	2.71
$E_{2v\_1NN}^f$ (eV)	4.96	5.17
$E_{2v\_2NN}^f$ (eV)	4.88	5.00
$E_{i\_100}^f$ (eV)	4.76	4.76
$E_{i\_110}^f$ (eV)	4.06	4.37
$E_{i\_111}^f$ (eV)	3.76	4.02
C_{11} (Gpa)	260.00	284.00* [10]
C_{12} (Gpa)	168.20	164.00* [10]
C_{44} (Gpa)	55.06	30.90* [10]
E_v^m (eV)	*0.54*	*0.45/0.55* [9]

Table S6 Summary of the lattice constant (l_A), cohesive energy (E_c), single and divacancy formation energies E_v^f and E_{2v}^f, interstitial formation energies (E_i^f) for various configurations, vacancy migration energy (E_v^m), and elastic constants of HCP Zr. Properties presented in *italics* were not used in the fitting dataset, and those denoted with an asterisk (*) correspond to experimental values.

Property	NbZrTi-EAM potential	DFT/experiment
l_A (Å)	3.23	3.23
E_c (eV)	6.32	6.28
E_v^f (eV)	1.77	1.94 [9]
E_{2v}^f (eV)	3.29	3.72 [9]
E_O^f (eV)	3.12	2.81 [11]
E_S^f (eV)	3.14	2.92 [11]
E_C^f (eV)	3.11	3.14 [11]
E_{BO}^f (eV)	2.99	2.70 [11]
E_{BS}^f (eV)	3.01	2.79 [11]
C_{11} (GPa)	133.40	143.40* [12]
C_{12} (GPa)	76.05	72.80* [12]
C_{44} (GPa)	29.22	32.00* [12]
E_v^m (eV)	*0.62*	*0.63* [9]

Table S7 Summary of the lattice constant (l_A), cohesive energy (E_c), single and divacancy formation energies E_v^f and E_{2v}^f, interstitial formation energies (E_i^f) for various configurations, vacancy migration energy (E_v^m), and elastic constants of HCP Ti. Properties presented in *italics* were not used in the fitting dataset, and those denoted with an asterisk (*) correspond to experimental values.

Property	NbZrTi-EAM potential	DFT/experiment
l_A (Å)	2.92	2.93
E_c (eV)	5.44	5.44
E_v^f (eV)	1.96	1.97 [9]
E_{2v}^f (eV)	3.62	3.74 [9]
E_O^f (eV)	2.62	2.40 [11]
E_S^f (eV)	2.79	2.65 [11]
E_C^f (eV)	2.62	2.82 [11]
E_{BO}^f (eV)	2.32	2.27 [11]
E_{BS}^f (eV)	2.41	2.46 [11]
C_{11} (GPa)	188.40	176.00 * [13]
C_{12} (GPa)	86.32	87.00 * [13]
C_{44} (GPa)	38.69	51.00 * [13]
E_v^m (eV)	*0.70*	*0.61* [9]

2.4.2 Binary alloys

Table S8, Table S9 and Table S10 present the energy properties of solute atoms and point defects in the Nb-Ti, Nb-Zr, and Zr-Ti binary alloys, respectively. As shown in Table S8, the formation energy of solute atoms in the Nb-Ti binary alloy deviates by no more than 0.03 eV from the DFT results, including the equiatomic Nb-Ti alloy. The vacancy formation energy is slightly lower than the DFT value, with a deviation within 0.3 eV. For interstitials, the Nb-Ti dumbbell configuration is most stable along the <111> direction, while the Ti-Ti dumbbell prefers the <100> direction, which is consistent with the DFT results.

In the Nb-Zr binary alloy, the formation energy of a single Zr solute atom differs from the DFT result by only 0.01 eV, while the formation energy for 50% Zr concentration is slightly overestimated by 0.12 eV. Both vacancy and interstitial formation energies agree well with DFT results: the Nb-Zr dumbbell interstitial favors the <111> orientation, while the Zr-Zr dumbbell tends to form along the <110> direction, with energy deviations less than 0.25 eV.

In the Zr-Ti binary alloy, the formation energy of the solute atom deviates by less than 0.01 eV from the DFT result. The vacancy and interstitial formation energies also show good consistency with DFT results, with energy deviations within 0.1 eV. Interstitials are predicted to preferentially form BO configurations. These results demonstrate that the optimized binary alloy potentials yield solute formation energies and point defect energetics in good agreement with DFT calculations, which is essential for accurately describing the thermodynamic and kinetic behaviors of defects in the NbZrTi medium-entropy alloy.

Table S8 Energy properties of Ti solutes and point defects in the Nb-Ti binary alloy using the EAM NbZrTi potential.

Property	NbZrTi-EAM （eV）	DFT（eV）
$E^{\mathrm{f}}_{\mathrm{sub-Ti}}$ (eV)	0.17	0.18
$E^{\mathrm{f}}_{\mathrm{sub-50\%Ti}}$ (eV)	4.96	4.93
$E^{\mathrm{f}}_{\mathrm{Ti-vac.,1NN}}$ (eV)	2.53	2.75
$E^{\mathrm{f}}_{\mathrm{Ti-vac.,2NN}}$ (eV)	2.52	2.82
$E^{\mathrm{f}}_{\mathrm{Nb-Ti,<111>}}$ (eV)	3.37	3.62
$E^{\mathrm{f}}_{\mathrm{Nb-Ti,<110>}}$ (eV)	3.88	3.74
$E^{\mathrm{f}}_{\mathrm{Nb-Ti,<100>}}$ (eV)	3.94	4.05
$E^{\mathrm{f}}_{\mathrm{Ti-Ti,<111>}}$ (eV)	3.30	3.24
$E^{\mathrm{f}}_{\mathrm{Ti-Ti,<110>}}$ (eV)	2.98	3.17
$E^{\mathrm{f}}_{\mathrm{Ti-Ti,<100>}}$ (eV)	3.67	3.52

Table S9 Energy properties of Zr solutes and point defects in the Nb-Zr binary alloy using the NbZrTi potential.

Property	NbZrTi-EAM	DFT
$E^{\mathrm{f}}_{\mathrm{sub-Zr}}$ (eV)	0.33	0.34
$E^{\mathrm{f}}_{\mathrm{sub-50\%Zr}}$ (eV)	9.76	9.64
$E^{\mathrm{f}}_{\mathrm{Zr-vac.,1NN}}$ (eV)	2.48	2.65
$E^{\mathrm{f}}_{\mathrm{Zr-vac.,2NN}}$ (eV)	2.93	3.17
$E^{\mathrm{f}}_{\mathrm{Nb-Zr,<111>}}$ (eV)	4.43	4.42
$E^{\mathrm{f}}_{\mathrm{Nb-Zr,<110>}}$ (eV)	4.86	4.74
$E^{\mathrm{f}}_{\mathrm{Nb-Zr,<100>}}$ (eV)	5.24	5.11
$E^{\mathrm{f}}_{\mathrm{Zr-Zr,<111>}}$ (eV)	5.38	5.13
$E^{\mathrm{f}}_{\mathrm{Zr-Zr,<110>}}$ (eV)	4.72	5.09
$E^{\mathrm{f}}_{\mathrm{Zr-Zr,<100>}}$ (eV)	5.37	5.51

Table S10 Energy properties of Ti solutes and point defects in the Zr-Ti binary alloy using the NbZrTi potential.

Property	NbZrTi-EAM	DFT
$E^{\mathrm{f}}_{\mathrm{sub-Ti}}$ (eV)	0.18	0.19
$E^{\mathrm{f}}_{\mathrm{sub-50\%Ti}}$ (eV)	4.88	4.89
$E^{\mathrm{f}}_{\mathrm{Ti-vac.,1NN}}$ (eV)	2.17	2.18
$E^{\mathrm{f}}_{\mathrm{Ti-vac.,2NN}}$ (eV)	2.14	2.17
$E^{\mathrm{f}}_{\mathrm{Zr-Ti\_inter.,<BO>}}$ (eV)	1.58	1.48
$E^{\mathrm{f}}_{\mathrm{Zr-Ti\_inter.,<O>}}$ (eV)	2.00	1.95
$E^{\mathrm{f}}_{\mathrm{Zr-Ti\_inter.,<S>}}$(eV)	2.13	2.20
$E^{\mathrm{f}}_{\mathrm{Ti-Ti\_inter.,<BO>}}$ (eV)	1.17	1.22
$E^{\mathrm{f}}_{\mathrm{Ti-Ti\_inter.,<O>}}$ (eV)	1.82	1.85
$E^{\mathrm{f}}_{\mathrm{Ti-Ti\_inter.,<S>}}$ (eV)	1.69	1.69

2.4.3 NbZrTi multi-principal alloys

The physical and defect properties of NbZrTi were also verified against DFT calculations, including lattice constant (see Table S11), local lattice distortion (see Fig. S8), vacancy formation energy, interstitial formation energy and vacancy migration energy of equiatomic NbZrTi (see Fig. S9). The lattice constant of NbZrTi agrees well with DFT result, and a large extent of local lattice distortion was observed from both calculations, with the EAM potential showing a slight overestimation. With the obtained potential, the vacancy formation energies for Nb, Zr, and Ti in NbZrTi are 1.37 eV ± 0.43 eV, 1.28 eV ± 0.46 eV, and 1.34 eV ± 0.44 eV, respectively. These values show relatively good agreement with the DFT calculation results[14]. Fig. S9 (b) presents the formation energies for various types of interstitials. The energy order for these interstitials is as follows: Ti-Ti (1.26 eV ± 0.40 eV) < Ti-Nb (1.44 eV ± 0.51 eV) < Ti-Zr (1.94 eV ± 0.52 eV) < other interstitial types (2.16 eV ± 0.51 eV). Owing to their relatively low occurrence in the final optimized structure, the Nb–Nb, Nb–Zr, and Zr–Zr interstitial configurations exhibit higher formation energies and are therefore grouped together as "other interstitial types". The formation energy sequence of all interstitial configurations predicted by the fitted potential is in agreement with DFT results, with energy deviations not exceeding 0.3 eV. As shown in Fig. S9 (c), the vacancy migration energies exhibit a wide distribution in the NbZrTi multi-principal element alloy,

with some values approaching 0 eV. This distribution is also consistent with the trends observed in DFT calculations[14].

Table S11 Lattice constants of Nb, Nb-1Zr, and NbZrTi from the DFT and EAM potential.

	EAM (Å)	DFT (Å)	Absolute Error (Å)
Nb	3.307	3.304	0.003
Nb-1Zr	3.309	3.306	0.003
NbZrTi	3.380	3.381	0.001

Comparisons of vacancy cluster formation and binding energies were also performed for Nb and NbZrTi using both the EAM and MTP potentials, as presented and discussed later in Section 4. With the EAM potential, the formation energy distributions for 9-vacancy and 10-vacancy clusters in NbZrTi are of similar magnitude to those from DFT. The cluster binding energy is also consistent with DFT calculations, with a difference less than 0.2 eV for 10-vacancy clusters.

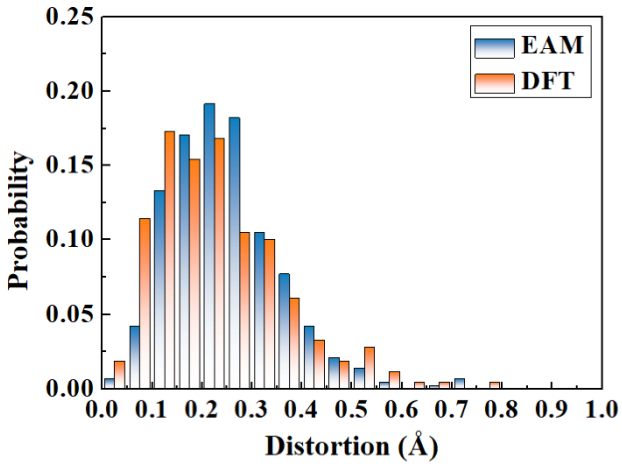

Fig. S8 Comparison of local lattice distortion in NbZrTi obtained from DFT calculations and the EAM potential.

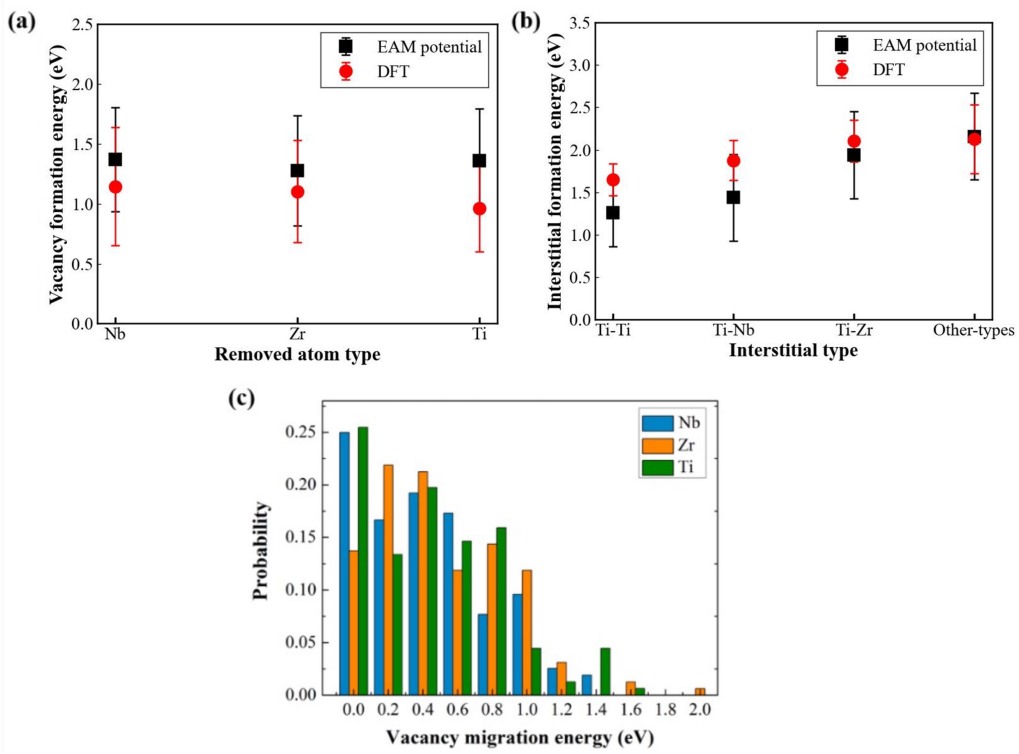

Fig. S9 Predicted point defect properties of NbZrTi multi-principal alloy using the developed EAM potential: (a) vacancy formation energy; (b) interstitial formation energy; (c) vacancy migration energy.

Furthermore, the melting points of pure Nb and NbZrTi were determined using both the single-phase and solid-liquid coexistence methods[20], resulting in values of 2783 K and 1933.5 K, respectively, as illustrated in Fig. S10. These values show good agreement with those obtained from experimental and phase diagram calculations (pure Nb: 2750 K; NbZrTi: 1960 K[5]). The optimized potential developed for the NbZrTi multi-principal element alloy in this study provides reliable and accurate predictions of point defect energetics in multi-principal element alloy systems. This lays an important foundation for subsequent research on the generation, distribution, and diffusion of defects in NbZrTi multi-principal element alloys.

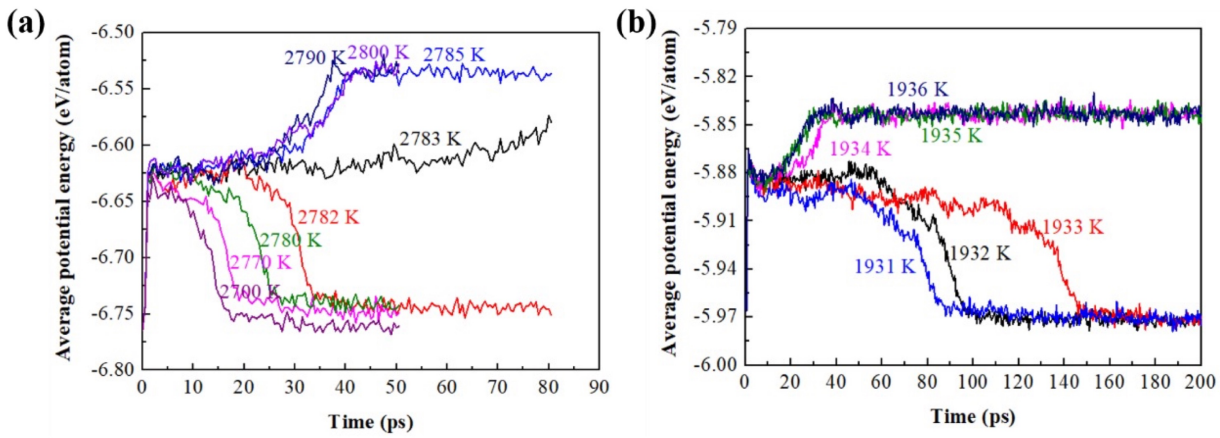

Fig. S10 The melting point calculations for pure Nb and NbZrTi by solid-liquid coexistence method: (a) pure Nb; (b) NbZrTi.

5

Section 3. Development of moment tensor potential (MTP) potential for NbZrTi multi-principal element alloy

3.1 Moment Tensor Potential

In contrast to empirically parameterized interatomic potentials that reply on fixed analytic functional forms (e.g., Lennard–Jones, EAM/MEAM), data-driven machine-learning potentials learn the potential-energy surface (PES) directly from high-fidelity reference data, yielding greater expressivity and transferability. Among these, the Moment Tensor Potential (MTP) uses a polynomial basis of moment-tensor invariants of the local environment[21]. The atomic energies are fitted via linear regression, achieving an optimal trade-off between accuracy and computational efficiency, while preserving translation, rotation, and permutation symmetries. Moreover, by increasing the basis order and cutoff radius, the representation is systematically improvable and can approximate any continuous, symmetry-invariant PES to arbitrarily high accuracy.

The total potential energy of the system is expressed as the sum of the local-environment energies of all atoms. Define the local environment n_i of the i-th atom to comprise the type of the central atom m_i, the type of its neighboring atoms m_j, and their relative position vectors $\boldsymbol{r_{ij}}$ (restricted to $|\boldsymbol{r_{ij}}|<R_{cut}$); then

$$E^{MTP} = \sum_{i=1}^{n} L(n_i). \tag{16}$$

The local energy $L(n_i)$ is linearly expanded using a set of symmetry-invariant basis functions B_α:

$$L(n_i) = \sum_\alpha c_\alpha \boldsymbol{B_\alpha}(n_i). \tag{17}$$

Here, $c = \{c_\alpha\}$ denotes the linear coefficients, obtained by fitting to the training data (energies, forces, and stresses).

To construct the specific form of B_α, the moment tensor is introduced as the descriptor. For each radial basis index μ and tensor order ν, the moment tensor of atom i is defined as:

$$M_{\mu,\nu}(n_i) = \sum_j f_\mu(|r_{ij}|, m_i, m_j) \underbrace{r_{ij} \otimes \cdots \otimes r_{ij}}_{\nu\ times}. \tag{18}$$

Here, $f_\mu(|r_{ij}|)$ is a radial basis function with the smooth cutoff at R_{cut}, and $\underbrace{r_{ij} \otimes \cdots \otimes r_{ij}}_{\nu\ times}$ is the angular term, which encodes the orientational (angular) information of the neighbors n_i.

In practical applications, the accuracy–efficiency trade-off of MTP is primarily governed by two hyperparameters: the maximum basis degree lev_{max}d the cutoff radius R_{cut}. The former controls the size of the invariant basis (and thus the number of trainable parameters), while the latter limits the extent of the local environment and directly affects model complexity and computational cost. In this study, lev_{max} and R_{cut}= 6 Å were employed to achieve a balanced compromise between accuracy and computational efficiency.

3.2 Validation of MTP potential

The complete training dataset for constructing the NbZrTi moment tensor potential (MTP) was generated from first-principles calculations using the VASP software. The projector-augmented wave (PAW) method and the Perdew–Burke–Ernzerhof (PBE) generalized gradient approximation were utilized for the exchange-correlation functional. A plane-wave cutoff energy of 450 eV was used, with Γ-centered k-point sampling at an average reciprocal-space resolution of ~0.03 $Å^{-1}$. Convergence thresholds were set to 10^{-4} eV for electronic iterations and 0.02 eV/Å for ionic relaxation.

Fig. S11(a) schematizes the MTP training workflow. *Ab initio* molecular dynamics (AIMD) simulations in the NVT ensemble were used to generate snapshot structures spanning compositions, temperatures, and strain states, thereby supplying diverse local environments for training. After sampling and model fitting, performance was assessed on a held-out test set not used during training; predictions for energies and forces are shown in Fig. S11(b, c). On this set, the coefficients of determination were R^2=0.9987 (energy) and R^2=0.9640 (force), with RMSEs of 3.4 meV/atom (energy) and 0.1142 eV $Å^{-1}$ (force). These metrics indicate excellent accuracy and generalization, supporting the use of the potential for simulations of more complex, service-relevant material systems.

The MTP was further tested by fitting energy-lattice-constant curves from both DFT and the MTP to the Birch–Murnaghan equation of state using a 4×4×4 SQS supercell (128 atoms) (Fig. S12). The fitted lattice constants are 3.382 Å (DFT) and 3.386 Å (MTP), demonstrating near-

quantitative agreement despite offsets in absolute energies. For the same configuration after relaxation, radial distribution functions from MTP and DFT nearly overlap over 0–10 Å. Together, these EOS and RDF benchmarks indicate that the MTP accurately reproduces both the equilibrium lattice parameter and short-range structure of NbZrTi. The same tests were conducted on Nb and Nb-1Zr, and the obtained lattice constants are shown in Table S12.

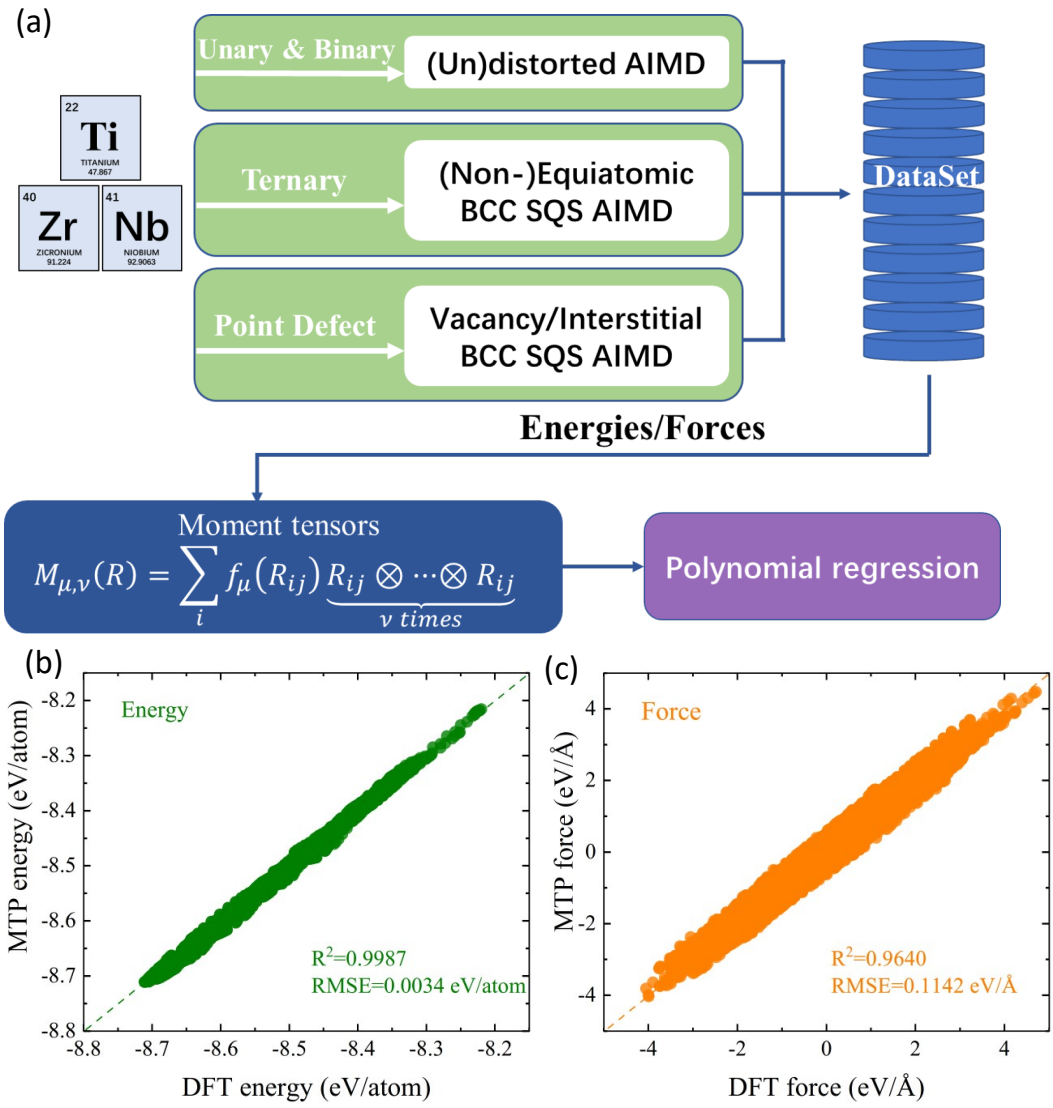

Fig. S11 Development and evaluation of the moment tensor potential (MTP). (a) Flowchart of constructing the moment tensor potential (MTP) for NbZrTi; Generalization performance of MTP on the (b) energy and (c) force test sets.

Table S12 Lattice constants of Nb, Nb-1Zr, and NbZrTi from the DFT and MTP potential.

	MTP (Å)	DFT (Å)	Absolute Error (Å)
Nb	3.306	3.304	0.002
Nb-1Zr	3.308	3.304	0.004
NbZrTi	3.382	3.386	0.004

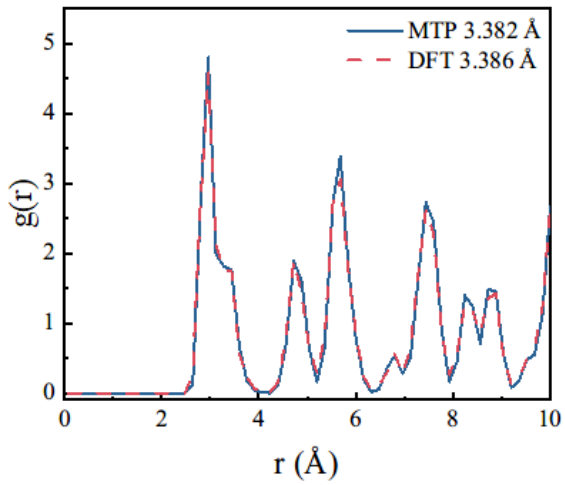

Fig. S12 Comparison of the MTP potential function and DFT for the structural characteristics of NbZrTi alloy. Lattice constants obtained from fitting based on the Birch–Murnaghan equation of state; Radial distribution function (RDF) curve after structural optimization.

Fig. S13 compares the elastic constants (C_{11}, C_{12}, C_{44}) calculated using the energy-strain method based on MTP potential and DFT, along with the derived bulk modulus, shear modulus, and Young's modulus. The results indicate that most elastic constants from MTP potential closely match those from DFT, with minor deviations[14]; similarly, the three macroscopic elastic moduli align well with DFT results. This comparison not only confirms the accuracy of MTP potential in predicting microscopic energies and forces but also demonstrates its ability to effectively characterize macroscopic elastic responses, making it suitable for large-scale mechanical behavior and multiscale simulations.

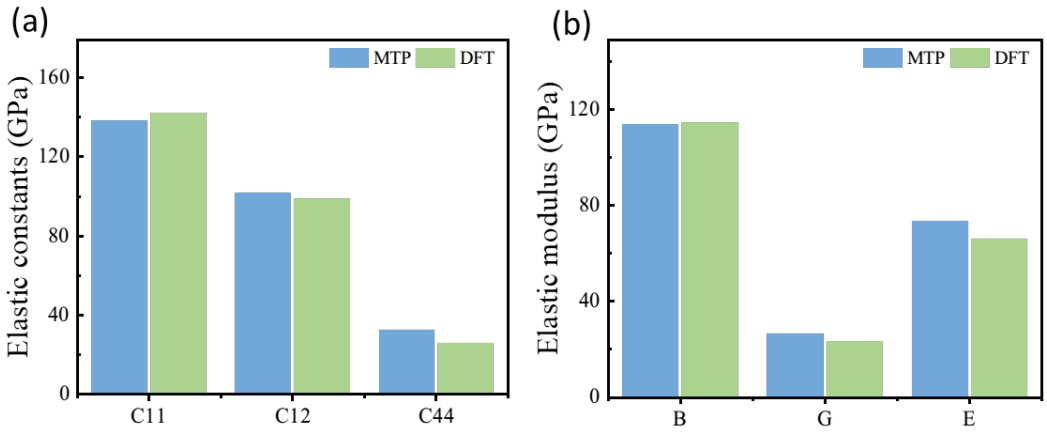

Fig. S13 The elastic properties of NbZrTi multi-principal alloy using the developed MTP potential and DFT: (a) elastic constants; (b) elastic modulus.

Table S13 Chemical Potential of Nb, Zr, Ti in NbZrTi from the DFT and MTP potential.

	MTP (eV)	DFT (eV)	Relative error (%)
Ti	-7.87	-7.87	0.12
Zr	-8.43	-8.42	0.05
Nb	-10.19	-10.17	0.21

The point defect properties of the NbZrTi alloy were verified using the MTP potential. The chemical potentials of each element were determined through the atomic substitution method, with DFT results as a benchmark; specific values are provided in Table S13. The findings show that the relative error in chemical potentials between MTP and DFT is less than 0.5%, indicating that the MTP reproduces chemical potentials with high fidelity.

After subtracting elemental chemical potentials, we evaluated formation energies of single vacancies, single interstitials, and vacancy migration barriers in NbZrTi (Fig. S14). The vacancy formation energies (mean ± SD) are Nb: 1.15 ± 0.56 eV, Zr: 1.01 ± 0.39 eV, and Ti: 1.03 ± 0.47 eV, in overall agreement with DFT (mean absolute deviation < 0.1 eV) [14]. For interstitials, the energetic ordering is Ti–Ti < Ti–Nb < Ti–Zr ~ others, with averages 1.56 ± 0.22 eV, 1.70 ± 0.24 eV, 1.91 ± 0.30 eV, and 1.88 ± 0.29 eV, respectively; the MTP reproduces both the DFT ranking and magnitudes with small deviations[14]. Due to higher energy, other types appear less frequently in MTP calculations, resulting in fewer formation energy than Ti-Zr. Vacancy migration energies

exhibit a broad distribution (Fig. S14) that mirrors the DFT trend[14]. Collectively, these benchmarks show that the MTP captures point-defect energetics and vacancy-mediated kinetics in NbZrTi with high fidelity and strong generalization.

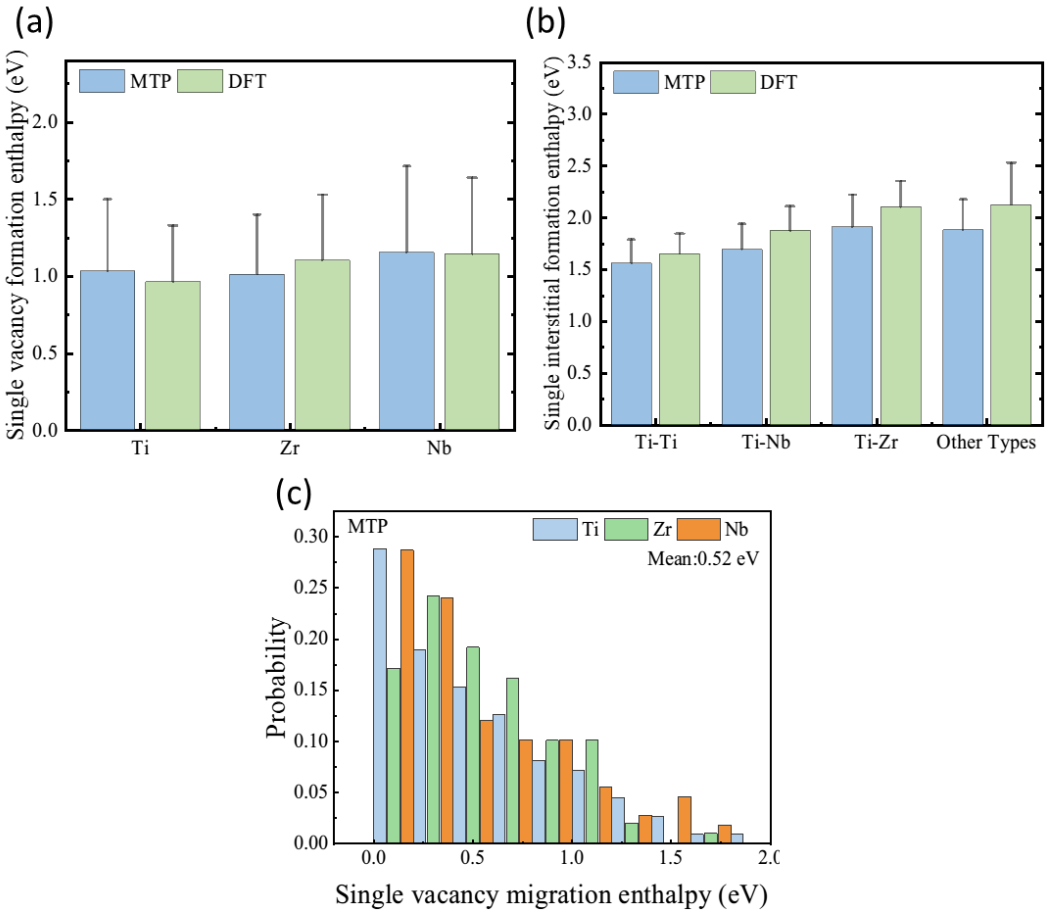

Fig. S14 Predicted point defect properties of NbZrTi multi-principal alloy using the developed MTP potential: (a) single vacancy formation energy; (b) single interstitial formation energy; (c) single vacancy migration energy.

Overall, our developed MTP for NbZrTi provides a robust and reliable machine learning potential that accurately predicts structural, mechanical, and defect properties. It demonstrates strong generalization capabilities and is well-suited for large-scale simulations of multi-component alloys, offering a solid foundation for studies on defect generation, distributions, and diffusion mechanisms in NbZrTi.

Section 4. First-principles validation of defect cluster properties

In order to verify that the developed potential can accurately describe the properties of vacancy clusters, DFT calculations were performed in a 300-atom supercell ($5a_0 \times 5a_0 \times 6a_0$) to determine the formation energies of 9-vacancy clusters, 10-vacancy clusters, as well as the binding energies of monovacancies to 9-vacancy clusters. The DFT calculations were performed with the VASP program. For NbZrTi, the random solid structure was constructed based the special quasi-random model (SQS) model[22]. The DFT settings are similar to those described in Section 2 of the Supplementary materials for the potential fitting database generation. The only difference is that, owing to the large supercell size, a single Γ-point was used for reciprocal space sampling. The most compact vacancy clusters were used as initial configurations, as shown in Fig. S15.

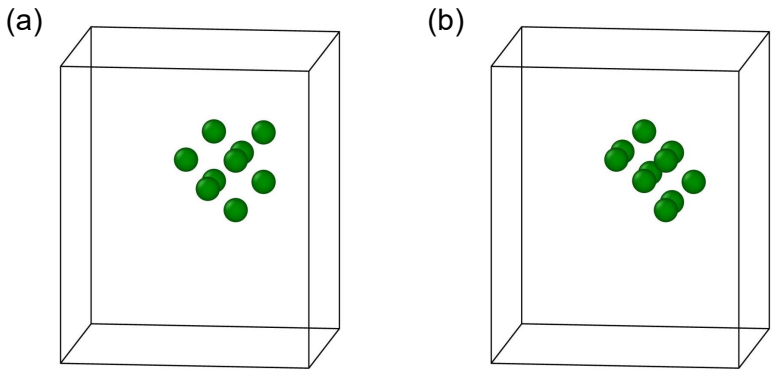

Fig. S15 Initial compact vacancy cluster configurations in DFT calculations：(a) 9-vacancy cluster，(b) 10-vacancy cluster.

The Widom-type substitution technique[23] was used to calculate the elemental chemical potential. A total of 32 atomic substitution sets were performed, comprising 8 Zr to Nb, Nb to Zr, Ti to Nb and Nb to Ti substitutions. Chemical potentials for Nb, Zr, and Ti are found to be -10.187 eV, -8.371 eV and -7.774 eV, respectively, which differ by less than 0.021 eV when compared with values obtained from a 108-atom supercell using a $3 \times 3 \times 3$ *k*-point mesh[14]. Average single vacancy formation energies were calculated based on 24 single vacancy configurations, with 8 configurations each for Nb, Zr and Ti atom removals. Twelve 9-vacancy and 10-vacancy clusters

were simulated at distinct supercell positions. Each 10-vacancy configuration was generated at the same position as its 9-vacancy counterpart.

The formation and binding energies of vacancy clusters from DFT calculations and interatomic potentials are presented in Table S14 for Nb and NbZrTi. The most compact volumetric configurations by minimization of surface area were compared. First, both potentials exhibit good agreement with DFT results for the binding energy of 10-vacancy clusters in pure Nb. Note that the standard deviation of the binding energy was obtained by first calculating each binding energy based on V_9 and V_{10} in the same local region. This takes into account the correlation between V_9 and V_{10} to avoid overestimation of the broadening effect. In NbZrTi, the formation energies using the EAM potential agree well with DFT results, demonstrating the EAM potential's capability to extrapolate to large vacancy clusters. At cluster sizes of 9 and 10, the EAM potential slightly overestimates the cluster formation energy and underestimates the energy fluctuation. Even with the underestimation of the energy broadening induced by the local chemical environment, there remains substantial overlap between the formation energies of V_{10} and V_9+V_1, indicating a strong driving force toward cluster dissociation.

Table S14 Energy of monovacancy and vacancy clusters in Nb and NbZrTi from the DFT, EAM potential, and MTP potential. The most compact cluster configurations were adopted for comparison.

Material type	**Energy**	**DFT (eV)**	**EAM (eV)**	**MTP (eV)**
Nb	$E^b(V_{10})$	1.26	1.31	1.37
NbZrTi	$E^f(V_1)$	1.16 ± 0.47	1.34 ± 0.44	1.07 ± 0.48
	$E^f(V_9)$	11.00 ± 1.59	10.81 ± 1.26	8.50 ± 2.42
	$E^f(V_1) + E^f(V_9)$	12.16 ± 1.66	12.15 ± 1.34	9.57 ± 2.47
	$E^f(V_{10})$	11.90 ± 1.35	11.76 ± 1.18	10.27 ± 2.85
	$E^b(V_{10})$	0.26 ± 1.52	0.39 ± 1.21	-0.70 ± 2.21
	$E^f(V_{20})$	/	19.81 ± 1.39	22.62 ± 3.20

For the MTP potential, although the vacancy cluster formation energy is underestimated at a cluster size of 10, it yields higher formation energies for larger clusters (n > 15) (see V_{20} in Table S11 and Section 6 of the Supplementary Materials), indicating greater predicted stability for these large clusters. Nonetheless, the binding energies of monovacancies to these large clusters still

approach zero (see Fig. S23 in Section 6), reflecting the suppressed tendency of cluster binding induced by variations in local chemical environment.

It is observed that during the DFT structural energy minimization, atom-vacancy exchanges can occur spontaneously, resulting in less compact configurations without thermal activation. Among these V_9 and V_{10} configurations, 16.7% of the vacancy clusters transformed into non-compact but not fully disassociated configurations, defined by each vacancy maintaining at least one neighbor vacancy ≤ 3NN (see Fig. S16(a)); 29.2% of the configurations evolved to dissociated configurations, where the minimum distance between vacancies exceeds 3NN (see Fig. S16(b)). This phenomenon of spontaneous atom-vacancy exchange is also in line with the behavior of cluster dissociation during high-temperature diffusion, as presented in Fig. 3 of the main article. A high probability of structural transformation at 0 K indicates zero or minimal energy barriers for vacancy–atom exchanges at these sites. With thermal activation, migration via low or moderate energy barriers can be further promoted, resulting in cluster dissociation during diffusion.

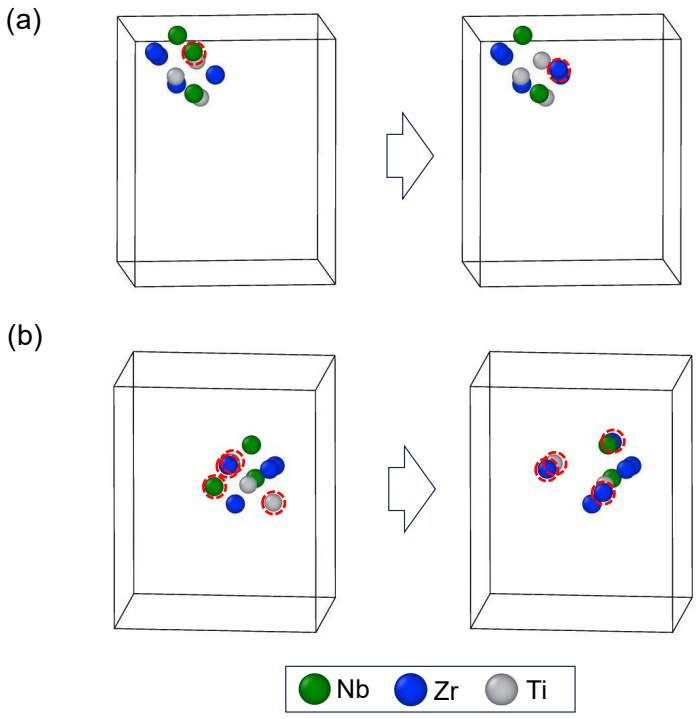

Fig. S16 Representative cases of structural relaxation of V_{10} clusters at 0 K: (a) relaxation to a non-compact configuration; (b) relaxation to a dissociated configuration.

For interstitial clusters, defect energies for cluster sizes of 4 and 5 were calculated in Nb and NbZrTi, as presented in Table S15. Ten sets of interstitial clusters were calculated in NbZrTi with Γ-centered *k*-point meshes of 2 × 2 × 2 for a supercell of 300 atoms. For defect structures, the system volume is scaled by the total number of atoms. The choice of cluster size is limited by the large stresses induced by interstitial clusters within a DFT-acceptable supercell.

Table S15 Energy of single interstitial and interstitial clusters in Nb and NbZrTi from the DFT and EAM potential. The Ti-Ti single interstitial formation energy was used for binding energy calculations.

Material type	**Energy**	**DFT (eV)**	**EAM (eV)**
Nb	$E^b(I_5)$	1.25	1.64
NbZrTi	$E^f(I_1)$	1.46 ± 0.23	1.26 ± 0.40
	$E^f(I_4)$	5.73 ± 0.73	5.73 ± 0.94
	$E^f(I_5)$	6.67 ± 0.52	6.77 ± 0.98
	$E^b(I_5)$	0.52 ± 0.70	0.23 ± 1.01

It can be seen that the binding energy of Nb agrees well with the DFT result. The formation energy in NbZrTi is mildly overestimated from the EAM potential. Note also that the DFT calculations also involve certain uncertainties due to the limited relaxation freedom in the small supercell. which prevents further reduction in the formation energy. Large cell simulations with the EAM potential indicate that even small interstitial clusters can undergo significant structural modifications and distort the lattice within a large impact region. Nevertheless, the formation energies of I_4 and I_5 and the binding energy of I_5 exhibit significant energy variations from the DFT calculations. Both methods yield small binding energies. Considering the energy broadening, it is also likely for I_5 clusters to reach negative binding energies, indicating a tendency of dissociation.

Section 5. Supplementary irradiation defect simulations using the EAM potential

Fig. S17 shows the vacancy cluster formation energy of the LCO structure annealed at 873 K using the EAM potential. A combined Monte Carlo (MC) + MD approach[24] was employed to obtain the LCO structure with a simulated annealing temperature of 873 K. In the 54000-atom supercell, MC swapping of 100 atom pairs was performed at intervals of 800 MD steps.

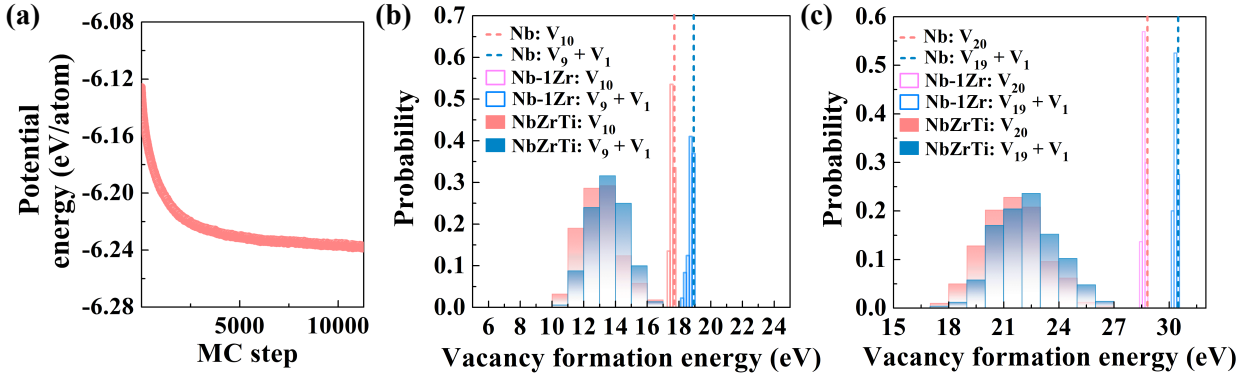

Fig. S17 Vacancy cluster formation energy in NbZrTi with the LCO structure annealed at 873 K using the EAM potential. (a) Variation of potential energy with MC steps during the generation of the LCO structure in NbZrTi. (b-c) Energy distributions of vacancy formation energies for representative cluster sizes of 10 and 20.

The extent of LCO is relatively weak due to the elevated temperature, as reflected by the small per-atom energy difference in Fig. S17 (a). The energy difference of –0.12 eV/atom relative to the RSS structure is of the same order as that reported in previous DFT calculations (–0.093 eV/atom at an annealing temperature of 800 K)[25]. Note that DFT simulations of LCO are also limited by the supercell size and atomic swapping times, which could further decrease the LCO structural energy. Accurately capturing such small energy differences from elemental rearrangement is relatively difficult for the classical potential while still maintaining an accurate description of defect properties. Nevertheless, it is evident that, similar to NbZrTi with the RSS structure, NbZrTi with the LCO structure also exhibits a large overlap in formation energies of *n*-vacancy clusters and the sum of (*n*–1) vacancy clusters plus single vacancies. This behavior can be attributed to the fact that the extent of LCO is not pronounced at the studied irradiation temperature[26], where atomic-level variations in chemical bonding strength remain the dominant influence.

Fig. S18(a) shows that the vacancy cluster formation energy correlates with the types of bonds removed from the cluster. Taking Nb–Nb bonds as an example, since they possess the highest overall bond strength, their substantial removal increases the total energy of the defect structure, resulting in a higher cluster formation energy. Fig. S18(b) shows that, in addition to the initial unrelaxed structure energy, a large extent of local structural relaxation also leads to a decrease in cluster formation energy. Depending on the local chemical environment, the degree of freedom for structural adjustment can differ for clusters at different sites. With the significant local lattice distortion in NbZrTi, differences in structural relaxation also result in variations in cluster formation energy.

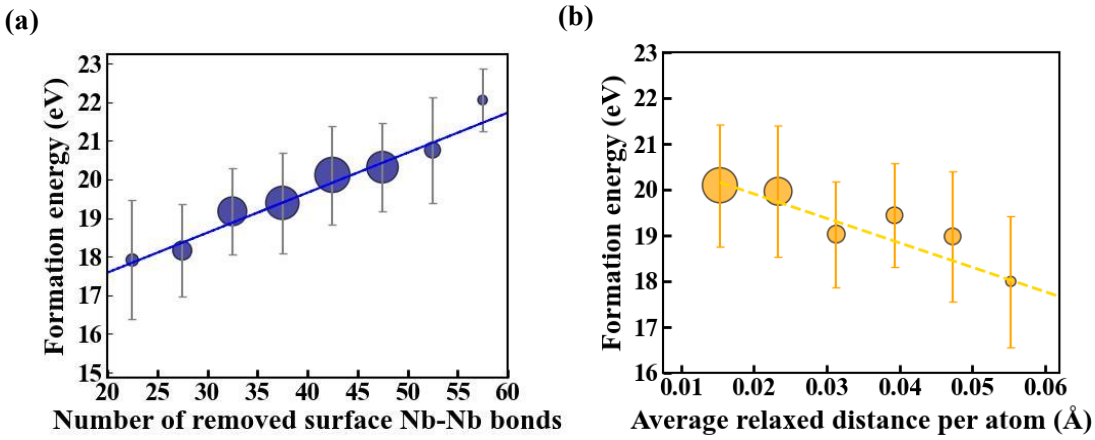

Fig. S18 (a) Vacancy cluster formation energy as a function of the number of cluster surface Nb–Nb bonds removed from the perfect structure for a cluster size of 20. (b) Vacancy cluster formation energy as a function of the average relaxed atomic distance for a cluster size of 20. The marker area is proportional to the number of defect configurations within each bin width.

In conventional BCC materials, a sphere-like structure is expected to minimize the surface energy, as clearly demonstrated by the correlation between the *n*-dependent Wigner-Seitz cluster surface area and the vacancy binding energy[27]. The case of NbZrTi turns out to be very different, as the atomic-level heterogeneity introduces two key effects. First, an identical compact vacancy cluster configuration can have distinct formation energies at different locations in the sample. This difference arises from site-dependent bond-breaking energy and from the different subsequent

energy reduction induced by the structural relaxation, thanks to the variable lattice distortion and bonding strengths at different sample locations[26]. Although lattice vibrations are pronounced at high temperatures, the variation in bond strength remains significant, as evidenced by the ICOHP analysis at 873 K (see Fig. S19). Second, from the energy reduction standpoint, the preference for certain local chemical bonds on the cluster surface outweighs the minimization of the cluster surface area, which is no longer directly proportional to the surface energy. Consequently, non-spherical, less compact structures can be thermodynamically more stable (see representative configurations in Fig. S16). This unlocks yet another degree of freedom for structural relaxation, which is non-existent in conventional metals and alloys. As a result of these effects, the energy distinction is largely diminished between compact and noncompact (even dissociated) configurations.

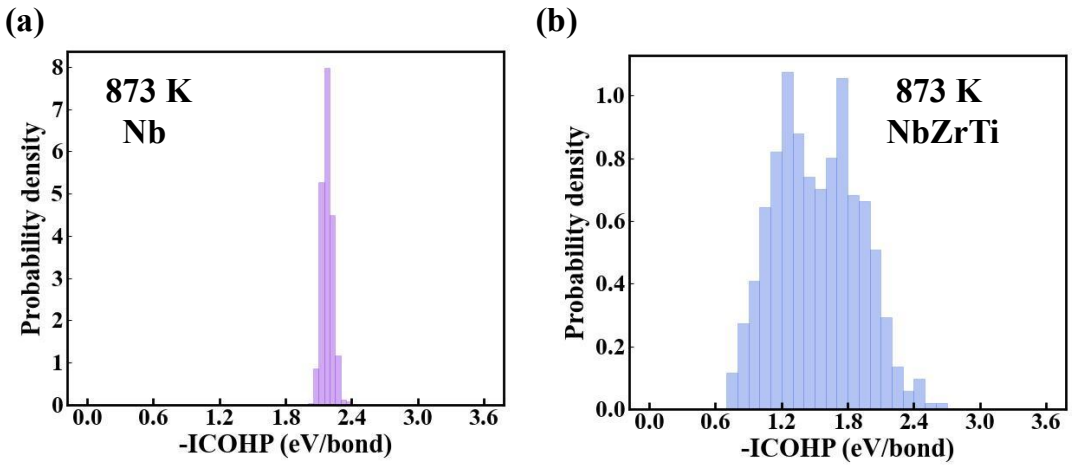

Fig. S19 Chemical bonding strength between first-nearest neighbors characterized by ICOHP analysis at 873 K in (a) Nb and (b) NbZrTi. AIMD simulations of the perfect structure vibrations were performed at 873 K, and ten independent random frames were selected from fifteen frames to calculate the average ICOHP values, ensuring that, for each atomic pair, the average distance equals the mean interatomic distance over the entire AIMD simulation. It is shown that in Nb, although the bond strength deviates from a fixed single value at 0 K, it still exhibits a narrow distribution. In contrast, a broad distribution of bond strength is maintained in NbZrTi at 873 K.

Fig. S20 illustrates that the 1/2<111> loop configuration possesses the lowest formation energy among the <100> loop, 1/2<111> loop, and spherical configurations, indicating its higher energetic stability.

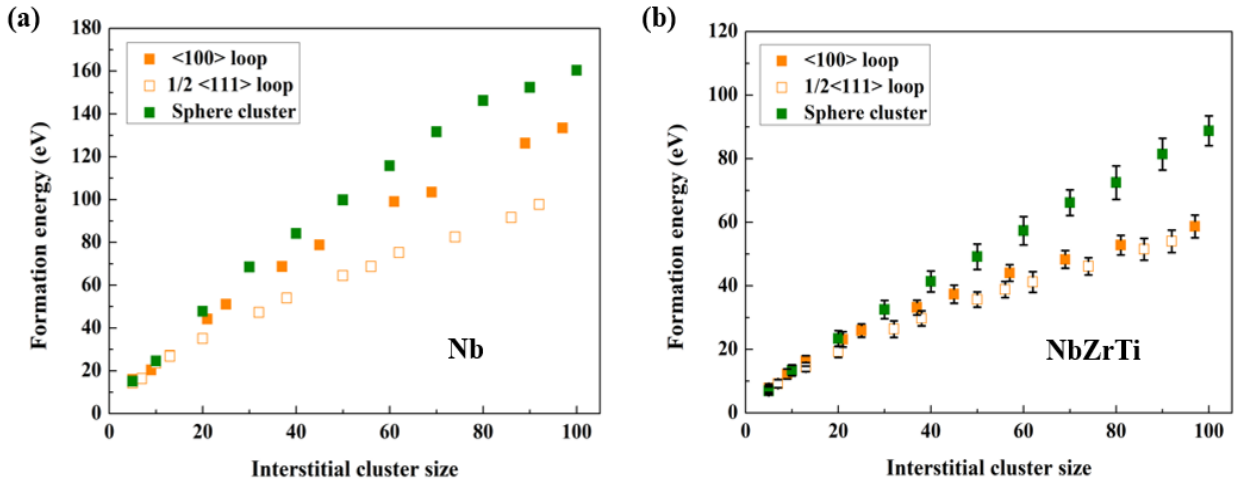

Fig. S20 Interstitial formation energies of <100> loops, 1/2<111> loops and spherical clusters: (a) pure Nb; (b) NbZrTi.

Fig. S21 presents the disassociation behavior of a 40-vacancy cluster. Compared to clusters of up to 20 vacancies studied in the main article, this larger cluster exhibits overall greater stability. However, as shown in Fig. S21(c) and (f), NbZrTi still shows a strong tendency to break into smaller clusters (sizes of 30 – 40), whereas the cluster sizes in Nb and Nb-1Zr remain at 39 – 40. We note that these results correspond to a relatively short diffusion time of 10 ns. As vacancy cluster instability persists across a wide range of cluster sizes in NbZrTi, an initial 40-vacancy cluster is expected to undergo further dissociation over longer timescales.

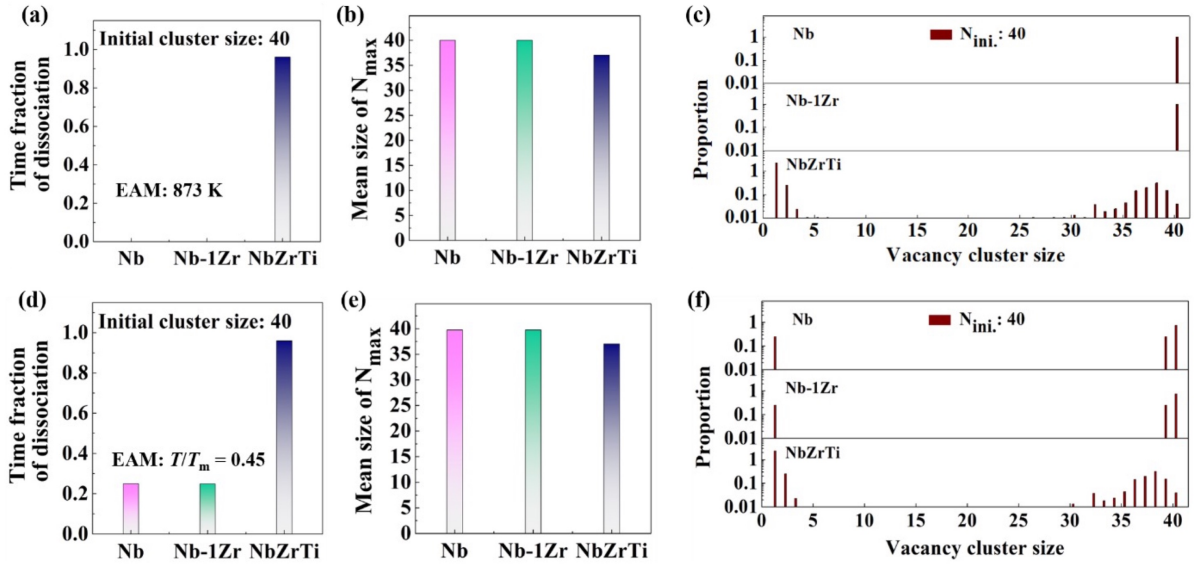

Fig. S21 Behavior of vacancy cluster diffusion for a cluster size of 40 at (a-c) 873 K and (d-f) 0.45 T/T_m (1252 K for Nb and Nb-1Zr; 873 K for NbZrTi), based on five independent 10-ns diffusion simulations. (a, d) Time fraction during which the vacancy cluster is in the dissociated state, where vacancies separated by more than 10 Å are treated as separate clusters. (b, e) Average size of the largest cluster during diffusion. (c, f) Vacancy size distribution during diffusion.

Fig. S22 shows the cluster size distributions for primary knock-on atom (PKA) energies ranging from 10 keV to 100 keV, in addition to those from 200-keV PKAs shown in the main text. It can be seen that NbZrTi consistently exhibits a significantly lower fraction of large vacancy clusters. As interstitials are generated near the cascade periphery, their cluster sizes are generally smaller than those of vacancies. In NbZrTi, the interstitial clusters are also reduced in size due to the lower binding energy, although the difference is less pronounced compared to vacancy clusters.

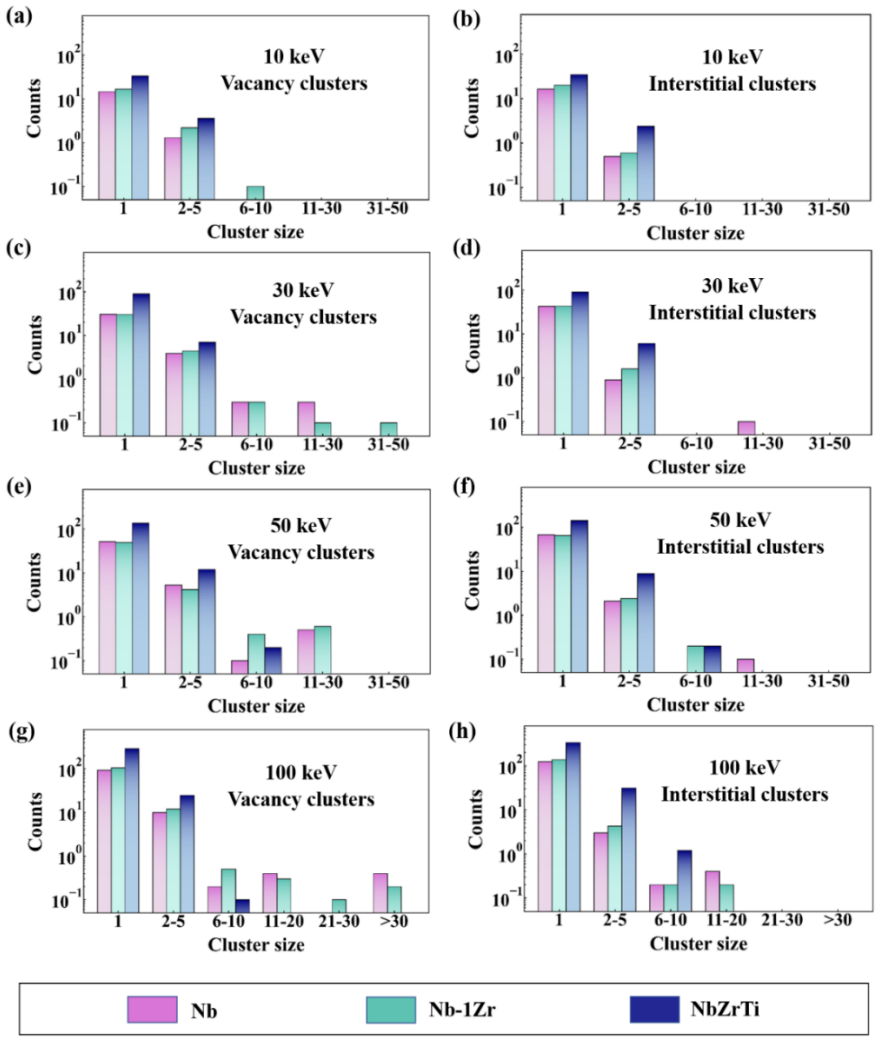

Fig. S22 Distribution of vacancy and interstitial clusters formed during the primary damage for PKA energies of (a, b). 10 keV, (c, d) 30 keV, (e, f) 50 keV and (g, h) 100 keV.

To provide an estimate of cluster size ranges for different irradiation conditions, 99.8% of PKAs are below 200 keV with 3-MeV Fe ion irradiation, and a Nb PKA of 200 keV corresponds to an incident neutron of 4.7 MeV, assuming maximum energy transfer in a head-on collision. Therefore, the simulated PKA energy range provides a broad and representative (though not complete) coverage of the PKA energies expected under typical irradiation conditions, including those in our ion irradiation experiments.

Section 6. Irradiation defect simulations using the MTP potential

Fig. S23 shows vacancy cluster formation and binding energies, computed with the MTP potential. Similar to the results from the EAM potential, vacancy clusters exhibit a broad formation energy distribution and binding energies in NbZrTi, indicating a suppressed tendency for vacancy cluster growth.

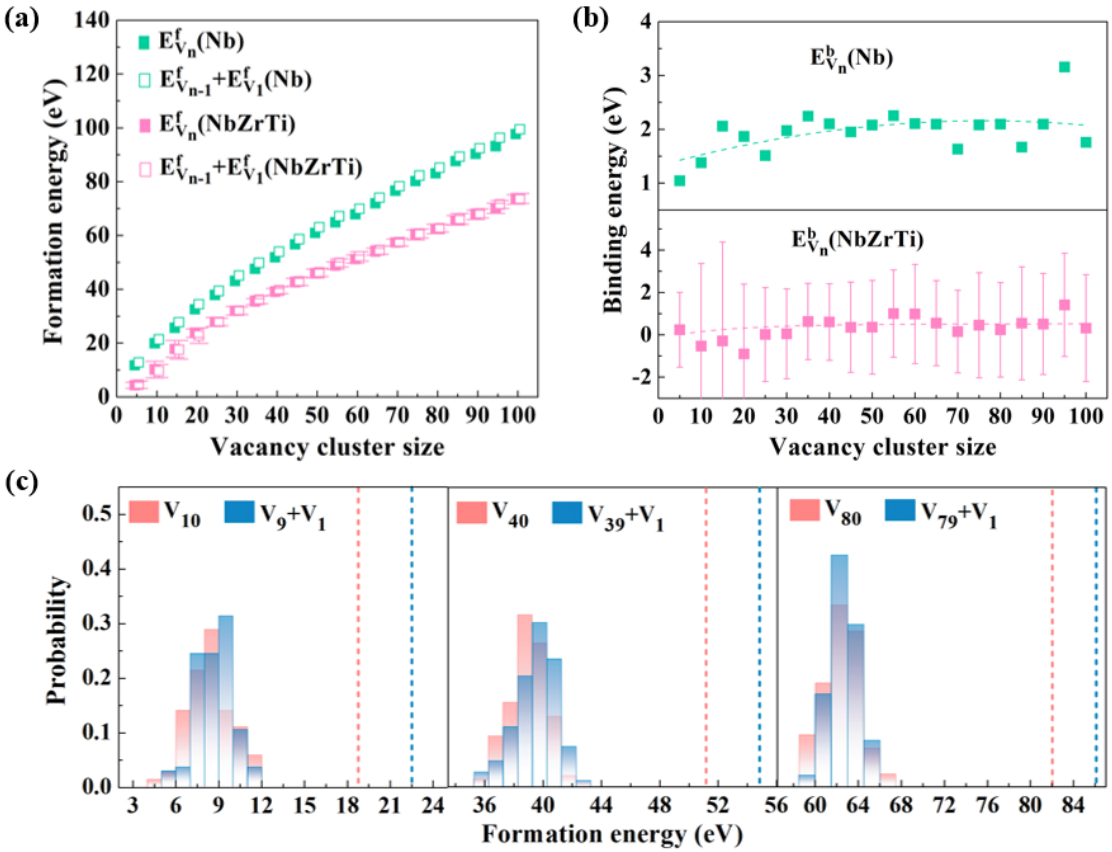

Fig. S23 Defect cluster formation energy and binding energy of the most compact configurations in Nb and NbZrTi using the MTP potential. (a) Formation energies of compact vacancy clusters of size n ($E^f_{V_n}$), and sum of formation energies for clusters of size n-1 ($E^f_{V_{n-1}}$) and monovacancies ($E^f_{V_1}$). (b) Binding energies of monovacancies in n-vacancy clusters. (c) Energy distributions of vacancy formation energies for representative cluster sizes.

Vacancy cluster stability was also assessed using the MTP potential through diffusion simulations of clusters of various sizes (see Fig. S24). Due to computational expense, the diffusion time was reduced to 5 ns per run with a total of five independent runs. It is evident that vacancy clusters in NbZrTi are more prone to dissociation, even at large sizes. By contrast, cluster stability in Nb and Nb–1Zr increases with size, following typical vacancy cluster behavior. Quantitative differences in dissociation probability and cluster size distribution relative to the EAM potential arise primarily from variations in energy predictions between the two potentials and differences in simulation durations. Nevertheless, both potentials show that vacancy clusters in NbZrTi can readily dissociate within a short diffusion time.

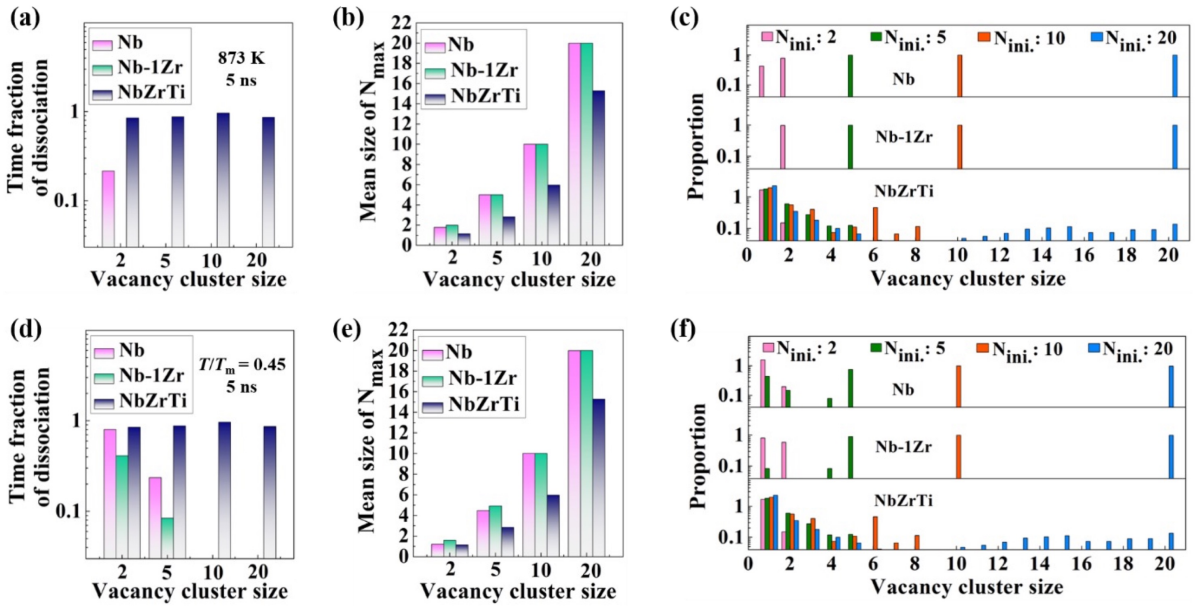

Fig. S24 Vacancy cluster stability during diffusion at (a-c) 873 K and (d-f) 0.45 T/T_m (1252 K for Nb and Nb-1Zr; 873 K for NbZrTi) using the MTP potential. (a, d) Time fraction during which the vacancy cluster is in the dissociated state, where vacancies separated by more than 10 Å are treated as separate clusters. (b,e) Average size of the largest cluster during diffusion. (c,f) Vacancy size distribution during diffusion. Five independent 5-ns diffusion simulations were performed for each condition.

Reference

1 Weber, W. J. & Zhang, Y. Predicting damage production in monoatomic and multi-elemental targets using stopping and range of ions in matter code: Challenges and recommendations. *Curr. Opin. Solid State Mater. Sci.* **23**, 100757 (2019).

2 Lin, Y.-R. *et al.* Predicting displacement damage for ion irradiation: Origin of the overestimation of vacancy production in SRIM full-cascade calculations. *Curr. Opin. Solid State Mater. Sci.* **27**, 101120 (2023).

3 Stoller, R. E. *et al.* On the use of SRIM for computing radiation damage exposure. *Nucl. Instrum. Methods Phys. Res., Sect. B* **310**, 75-80 (2013).

4 Loomis, B., Taylor, A. & Gerber, S. Void swelling of Nb and Nb-1% Zr induced by $58Ni^{+}$ bombardment. *J. Nucl. Mater.* **56**, 25-37 (1975).

5 Lederer, Y., Toher, C., Vecchio, K. S. & Curtarolo, S. The search for high entropy alloys: a high-throughput ab-initio approach. *Acta Mater.* **159**, 364-383 (2018).

6 Wadley, H., Zhou, X., Johnson, R. & Neurock, M. Mechanisms, models and methods of vapor deposition. *Prog. Mater Sci.* **46**, 329-377 (2001).

7 Zhou, X. *et al.* Atomic scale structure of sputtered metal multilayers. *Acta Mater.* **49**, 4005-4015 (2001).

8 Yao, B., Liu, Z. & Zhang, R. EAPOTc: An integrated empirical interatomic potential optimization platform for compound solids. *Comput. Mater. Sci* **211**, 111551 (2022).

9 Zhang, P., Li, Y. & Zhao, J. Materials selection for nuclear applications in view of divacancy energies by comprehensive first-principles calculations. *J. Nucl. Mater.* **538**, 152253 (2020).

10 Trivisonno, J., Vatanayon, S., Wilt, M., Washick, J. & Reifenberger, R. Temperature dependence of the elastic constants of niobium and lead in the normal and superconducting states. *J. Low Temp. Phys.* **12**, 153-169 (1973).

11 Verite, G. *et al.* Self-interstitial defects in hexagonal close packed metals revisited: Evidence for low-symmetry configurations in Ti, Zr, and Hf. *Phys. Rev. B.* **87**, 162-168 (2013).

12 Fisher, E. R., C. Single-crystal elastic moduli and the hcp->bcc transformation in Ti, Zr, and Hf. *Phys. Rev.* **135** (1964).

13 Simmons, G. Single crystal elastic constants and caluculated aggregate properties. *A handbook* **4** (1971).

14 Shi, T. *et al.* Distinct point defect behaviours in body-centered cubic medium-entropy alloy NbZrTi induced by severe lattice distortion. *Acta Mater.* **229**, 117806 (2022).

15 Yao, B., Liu, Z. & Zhang, R. EAPOTs: An integrated empirical interatomic potential optimization platform for single elemental solids. *Comput. Mater. Sci* **197**, 110626 (2021).

16 Starikov, S. & Smirnova, D. Optimized interatomic potential for atomistic simulation of Zr-Nb alloy. *Comput. Mater. Sci* **197**, 110581 (2021).

17 Zhao, Z., Yi, M., Guo, W. & Zhang, Z. General-purpose neural network potential for Ti-Al-Nb alloys towards large-scale molecular dynamics with ab initio accuracy. *Phys. Rev. B* **110**, 184115 (2024).

18 Roberge, R. Lattice parameter of niobium between 4. 2 and 300K. *J. Less-Common Met.;(Switzerland)* **40** (1975).

19 Kittel, C. & McEuen, P. Introduction to solid state physics, vol 8 Wiley New York. (1976).

20 Hong, Q. J. & Van De Walle, A. Solid-liquid coexistence in small systems: A statistical method to calculate melting temperatures. *J. Chem. Phys.* **139** (2013).

21 Novikov, I. S., Gubaev, K., Podryabinkin, E. V. & Shapeev, A. V. The MLIP package: moment tensor

potentials with MPI and active learning. *Mach. Learn.: Sci. Technol.* **2**, 025002 (2020).
22 Zunger, A., Wei, S.-H., Ferreira, L. G. & Bernard, J. E. Special quasirandom structures. *Phys. Rev. Lett.* **65**, 353 (1990).
23 Widom, B. Some topics in the theory of fluids. *J. Chem. Phys.* **39**, 2808-2812 (1963).
24 Ibrahim, S. A. *et al.* Effect of local chemical order on monovacancy diffusion in CoNiCrFe high-entropy alloy. *J. Nucl. Mater.* **601**, 155335 (2024).
25 Shi, T. *et al.* Spatial inhomogeneity of point defect properties in refractory multi-principal element alloy with short-range order: A first-principles study. *J. Appl. Phys.* **133** (2023).
26 Xun, K. *et al.* Local chemical inhomogeneities in TiZrNb-based refractory high-entropy alloys. *J. Mater. Sci. Technol.* **135**, 221-230 (2023).
27 Hou, J., You, Y.-W., Kong, X.-S., Song, J. & Liu, C. Accurate prediction of vacancy cluster structures and energetics in bcc transition metals. *Acta Mater.* **211**, 116860 (2021).